Influence of Lift-Induced Upwash on Propeller Blade Deformation: A Digital Image Correlation Study for Next-Generation Open Rotor Engines

Measurement Methodology and Results

Master Thesis

Edoardo Gamba

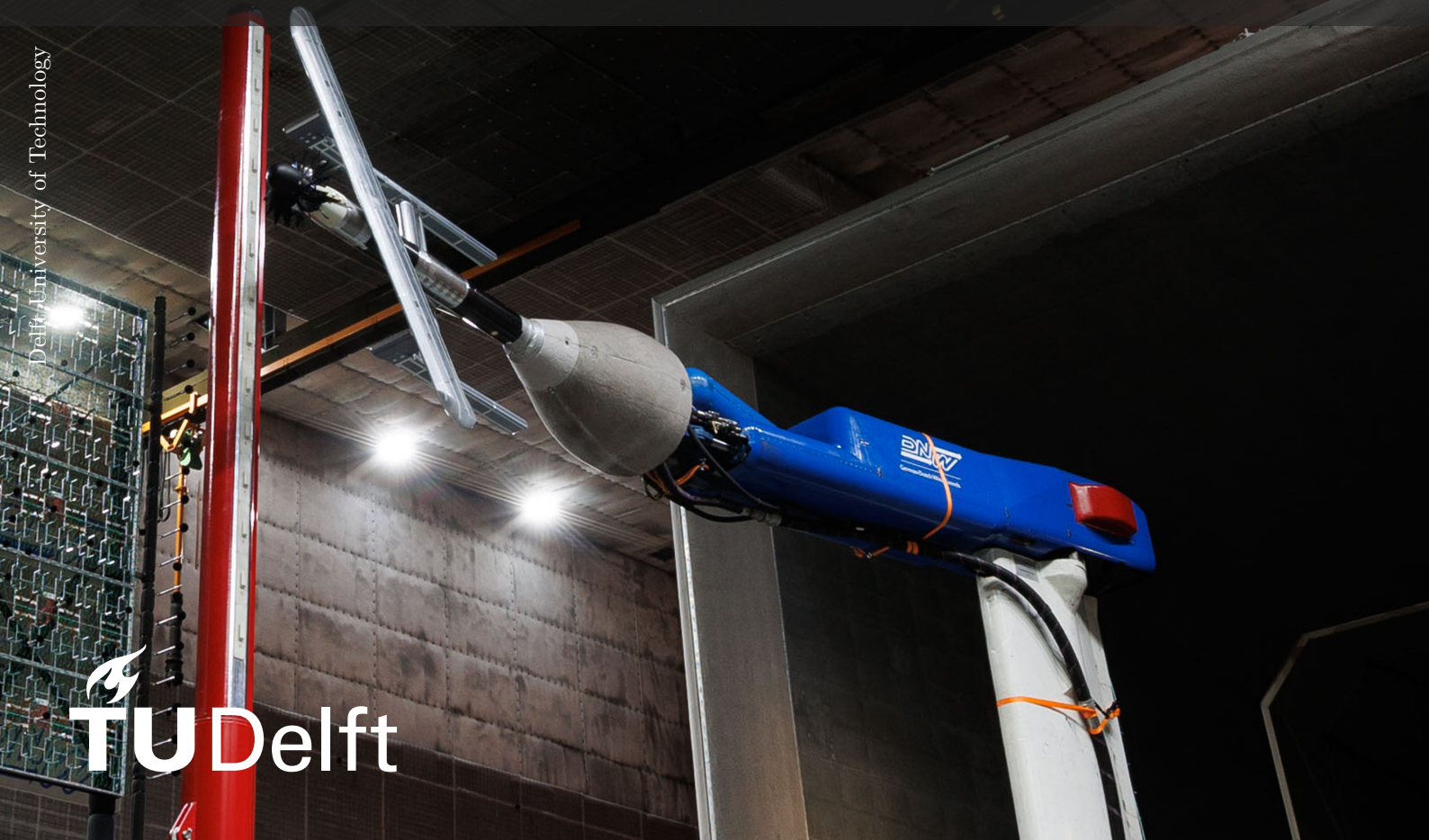

Delft University of Technology

TU Delft

Influence of Lift-Induced Upwash on Propeller Blade Deformation: A Digital Image Correlation Study for Next-Generation Open Rotor Engines

Measurement Methodology and Results

by

Edoardo Gamba

to obtain the degree of Master of Science
at the Delft University of Technology,
to be defended publicly on March 20th, 2025 at 10:00 AM.

Student number:	5844339	
Project duration:	April 15th, 2024 – March 7th. 2025	
Thesis committee:	Dr.Ing. T. Sinnige,	TU Delft, supervisor
	Ing. T. Kirmse,	DLR, supervisor
	Em. Prof. Dr.Ing. G. Eitelberg,	TU Delft, chairman
	Dr. A. Sciacchitano,	TU Delft

Deutsches Zentrum für Luft- und Raumfahrt
German Aerospace Center
DLR
TU Delft

Acknowledgements

I would like to express my gratitude to those who have supported me throughout this journey.

My heartfelt thanks go to Edoardo and Marco—without whom I would not be here graduating today. I am also deeply grateful to my supervisor Tomas, who gave me the opportunity to play with a serious wind tunnel for the first time at the LTT here in Delft.

I extend my appreciation to my colleagues Daniel, Jürg, and Mario, with whom I had the pleasure of working in Emmen at the LWTE. Through them, I had the chance to meet Tania and Jan, my current colleagues at DLR. Thank you both for everything you taught me, for the time spent together, and especially for the immense trust you placed in me during that week alone on shift at the LLF—it truly meant a lot.

Many thanks to Iris, Daniel, Alex, and everyone at Airbus with whom I had the pleasure of working in Marknesse. I am especially grateful for the data, without which this thesis would not exist.

To Marco and his moka pot, which made Göttingen feel a little more like home.

And, of course, to my family — who are probably exhausted from lunchtime thermodynamics lectures and once thought having me back for a few months couldn't be that bad. They're now eagerly counting down the days until I leave again.

Edoardo Gamba
Delft, March 2025

Summary

The present study investigates the deformation of propeller blades in the presence of a wing, specifically analysing the lift-induced upwash effects through experimental measurements conducted in a wind tunnel. The objective is to quantify the impact of non-uniform inflow on blade bending, with a particular focus on the aerodynamic interactions between the rotor and the wing. Image Pattern Correlation Technique (IPCT) was employed to measure blade deformation, leveraging high-resolution optical methods to capture structural response under varying flight conditions.

The experimental campaign was conducted at the Large Low-speed Facility (LLF) of the German-Dutch Wind Tunnels (DNW), a closed-circuit wind tunnel with an open test section measuring 6×8 m. The facility provides high flow uniformity, low turbulence levels, and a Mach number range up to 0.2, allowing for detailed aerodynamic and structural measurements. A range of rotor pitch angles and operating conditions were tested to assess how blade deformation varies with changes in aerodynamic loading. Preparatory work was done at DLR in Göttingen to test all the necessary assumptions.

Results indicate that inflow incidence angle (α_C) corrections, which account for the effective angle of attack due to the lift-induced upwash at the rotor, effectively account for deformation effects, including in swept-wing configurations. The propwash was found to significantly influence the wing lift and consequently the induced upwash and angle of attack at the rotor. The location of maximum bending, defined as the displacement normal to the plane defined by the rotor span and its root chordline, was verified for both the wing-on and wing-off cases, with the wing sweep being directly responsible for an increase in mean bending and a clockwise rotation in the deformation distribution. Furthermore, measurements revealed that the upgoing blade, closer to the wing leading edge, exhibited larger deviations between clean and wing-on setups due to both the rotation of the deformation distribution and to the increase in deformation which were not accounted for by the lift-induced α correction computed for the rotor centre. The effect of the component of lift-induced upwash field due to the wing sweep resulted in a 10% increase in mean bending at the worst case scenario of high angle of attack and advance ratio.

These results highlight the importance of wing-rotor integration for aerodynamic efficiency and structural resilience, particularly in higher disk loading configurations, such as open-rotor designs. The findings suggest that wing sweep and propwash interactions, identified as the main cause of the non-uniform inflow component, strongly influence blade deformation and could be relevant for future propulsion system designs. This has implications not only for structural analysis, as the rotor is more stressed, but also for aerodynamics, as the measured displacement can affect the twist distribution.

Strain gauges were considered a complementary method to digital image correlation, offering data to correlate IPCT measurements across the rotor disk and reconstruct deformation fields in occluded areas. Furthermore, linking in-plane loads from the RSB with rotor disk deformation could improve the understanding of blade behaviour.

The study also underscores the feasibility of using optical measurement techniques for partially occluded stator blades, provided that phase-dependent rotor wake effects on deformation remain negligible. In the investigated configuration with steel stator blades, deformation appeared negligible, falling within the measurement accuracy range. Future work should focus on integrating strain gauge data with IPCT to improve measurement coverage, exploring correlations between vibrational modes and blade deformation. These advancements would refine predictive aerodynamic models, provide insight into rotor-wing interactions and contribute to the development of more efficient propulsion systems for next-generation aircraft.

Contents

List of Figures

List of Tables

Nomenclature

Abbreviations

Abbreviation	Definition
1P	In-Plane Propeller Loads
ACS	Aircraft Simulator
APS-H	Camera Sensor Size (28mm)
BNC	Bayonet Neill–Concelman (Coaxial cable connector)
BPR	Bypass Ratio
C12	Stereo group of cameras 1 and 2
C34	Stereo group of cameras 3 and 4
CAD	Computer Aided Design
CFD	Computational Fluid Dynamics
CROR	Counter-Rotating Open-Rotor
DLR	Deutsches Zentrum für Luft- und Raumfahrt
DNW	German-Dutch Wind Tunnels
DOF	Depth of Field
IPCT	Image Pattern Correlation Technique
LLF	Large Low-Speed Facility
NLR	Netherlands Aerospace Center
PIV	Particle Image Velocimetry
REA54	Current test campaign
RBT	Rigid Body Transformation
RSB	Rotating Shaft Balance
SNR	Signal-to-Noise Ratio
SRV	Swirl-Recovery Vanes
STM	Standalone Trigger Module
TSFC	Thrust Specific Fuel Consumption
TTL	Transistor-Transistor Logic

Symbols

Symbol	Definition	Unit
BPF	Blade Passing Frequency	[Hz]
c	Chordlength	[m]
coc	Circle of Confusion Diameter	[mm]
c_L	Sectional Lift Coefficient	[-]
c_P	Pressure Coefficient	[-]
D	Rotor Diameter	[m]
d_0	Focus Distance	[m]
d_{dot}	Dot Diameter	[mm]
E_t	Triangulation Error	[px]
F_Z	Vertical In-Plane Force	[N]
f	Focal Length	[m]
J	Advance Ratio	[-]
M	Magnification Ratio	[-]
Ma	Mach Number	[-]
N	Lens Aperture	[-]
n	Revolutions per Second	[-]
rpm	Revolutions per Minute	[-]
rpm_C	Corrected Revolutions per Minute	[-]
Re	Reynolds Number	[-]
T	Thrust	[N]
T_{lvl}	Thrust Level	[-]
t	Exposure Time	[μs]
V_∞	Inflow Velocity	[m/s]
w	Vertical Upwash Component	[m/s]
α	Angle of Attack	[°]
α_{C}	Inflow Angle Correction	[°]
α_{eff}	Effective Inflow Angle	[°]
α_{G}	Geometric Inflow Angle	[°]
$\alpha_{\mathrm{Nonlinear}}$	Nonlinear Component of the Inflow Angle	[°]
α_{Vgrad}	Vertical Gradient Component of the Inflow Angle	[°]
β_p	Blade Pitch at 70% r/R	[°]
Γ	Circulation	[m^2/s]
η	Relative Wingspan Location	[-]
Λ	Wing Sweep	[°
φ	Blade Azimuth Angle	[°]
$\sigma(d_y)$	Bending Standard Deviation	[mm]

1

Introduction

1.1. Context and Importance of Propeller Deformation Study

The aviation industry is actively seeking technological advancements to reduce emissions and enhance fuel efficiency, driven by the global transition towards cleaner air transport. A key approach to achieving these goals is the increase in bypass ratios within propulsion systems, with two primary configurations emerging: high-bypass turbofan engines and open rotor systems. While high-bypass engines have substantially improved fuel efficiency, their further optimisation is constrained by the additional weight and aerodynamic drag associated with larger nacelles.

Open-rotor engines present a viable alternative by eliminating the nacelle, enabling larger rotor blades and achieving higher bypass ratios. This design is anticipated to result in a 10–20% reduction in fuel consumption compared to conventional turbofans (Guynn et al., 2012). However, as blade diameters increase, for a fixed rpm, the tip speeds also rise, which would lead to a reduction in the advance ratio and potentially cause supersonic flow at the blade tips. This phenomenon generates shock waves that degrade propeller efficiency, induce vibrations, and elevate noise levels. To avoid the decrease in advance ratio and mitigate these effects the fan of an open-rotor engine must operate at a lower rpm and therefore sustaining higher aerodynamic loads. Consequently, these engines feature an enlarged rotor disk to enhance bypass ratio, increased disk loading resulting from higher blade loading and solidity, and highly swept blades to reduce wave drag and prevent as much as possible shock formation.

The concept of open-rotor engines is not new; initial prototypes emerged in the 1980s as a response to escalating fuel costs during the oil crisis. Counter-Rotating Open Rotor (CROR) engines have been extensively studied and developed over the years, with research efforts focusing on their aerodynamic performance, noise characteristics, and structural integrity (Hoff, 1990; Negulescu, 2013; Stürmer et al., 2012).

The significance of deformation in blade design lies in its impact on both structural and aerodynamic performance. The blade must be engineered to withstand cyclic loading while preserving its intended aerodynamic efficiency. However, the shape of the blade in the jig does not match its deformed shape under operational conditions. This discrepancy results in a change in twist distribution, which must be inversely computed to ensure that, when loaded, the blade deforms into its optimal shape. This computation ensures that the blade performs as designed, maintaining both structural integrity and aerodynamic efficiency in real-world conditions.

While the bending itself does not have a strong aerodynamic effect, the twist distribution can substantially alter blade performance. The bending and twist are partially correlated, and their relationship depends on the blade's stiffness and shape. These measurements verify that the blade deforms as predicted, ensuring that all stress components are accounted for and that the blade shapes simulated in Computational Fluid Dynamics (CFD) match the results from experimental tests.

Figure 1.1: The General Electric *GE36*, first tested in 1985

Notable early examples include the *GE36* (Figure 1.1) by General Electric and Snecma (now SAFRAN), and the *578-DX* developed by Pratt & Whitney and Allison, both featuring counter-rotating blades in a pusher configuration.

The GE36, in particular, achieved a 33% reduction in TSFC (Thrust-Specific Fuel Consumption) compared to the Pratt & Whitney JT8D-17 engines typically installed on the 727 test aircraft (Sutcliffe, 1987).

The latest prototype under development is the *CFM Rise*, which incorporates an open rotor design combined with a variable pitch stator instead of a counter-rotating configuration. This approach eliminates the need for a gearbox and positions the fan on the cold side of the engine. Unlike the propfan concepts of the 1980s, where cabin noise concerns led to tail-mounted designs such as those proposed for the Boeing 7J7 and tested on the MD-80 and 727, the *CFM Rise* aims to replace pylon-mounted turbofans under the wings, benefiting from advancements in noise mitigation.

One of the many factors influencing the deformation of both rotor and stator is their interaction. The stator is subjected to the fluctuating induced velocity of the rotor wake and its tip vortices. Despite efforts to reduce stator loading by decreasing its diameter below the slipstream radius at its location, these vortices still contribute to the unsteady component of the load (Li et al., 2016; Avallone et al., 2019). Conversely, the stator's thrust modifies the flow around the rotor, resulting in effects analogous to those observed in turbomachinery (Dring et al., 1982), though with a considerably lower blade count and greater rotor-stator spacing.

The absence of an outer nacelle, which typically stabilises inflow to the fan, renders open rotor blades more susceptible to variations in incoming airflow. These variations stem from factors such as aircraft angle of attack and wing-to-pylon geometry. A non-uniform inflow across the propeller disk leads to uneven blade loading, introducing vibrations. If these vibrations coincide with the blade's natural frequencies, resonance effects may amplify them, posing risks of structural fatigue or even catastrophic failure.

One of the primary contributors to inflow angle non-uniformity is the lift-induced upwash generated by the aircraft wing, together with the geometrical mounting angle α_{G}. The relative positioning of the propeller disk with respect to the wing, as well as variations in lift magnitude, significantly alter the flow conditions experienced by the rotor blades (Veldhuis et al., 2013). The different modes and magnitudes of the blade deformations over the rotor disk influence the twist distribution, introducing a further cause for a difference in performance between the isolated and installed engine. Understanding and mitigating these effects is an important factor in optimising open rotor propulsion systems and enhancing their overall performance.

1.2. Project overview

The test campaign providing the data for this research is a collaboration between Airbus and Safran, partially funded by the European Clean Sky initiative. The campaign is designed to investigate the integration of an open-rotor engine with the aircraft simulator (ACS), comprised of a movable wing with interchangeable high lift devices, focusing on aerodynamic and aeroacoustic performance. The German Aerospace Center (DLR) is responsible for measuring the deformation of the rotor blades, along with developing a new methodology to capture the deformation of the stator with image correlation, which is often visually obstructed by the rotor blades during testing.

All of the data used in this thesis is derived from the common part of the test, which is publicly funded. This deformation data helps in checking the consistency of Airbus's and SAFRAN's internal models. It is correlated with Finite Element Analysis (FEA), CFD, and Fluid-Structure Interaction (FSI) simulations to ensure the models align with real-world behaviour and performance. No correlation is done with this computed data as it was not publicly available.

2

Literature review

The advancement of CFD and non-intrusive wind tunnel testing techniques, such as Particle Image Velocimetry (PIV), has significantly improved research on wing-propeller interaction. These methodologies have facilitated the development of interference models aimed at optimising the propulsor efficiency while enhancing the wing's lift-to-drag ratio by balancing the often conflicting design requirements of both components.

Another crucial aspect of this interaction is the effect of propeller loads on blade deformation. The combined influence of aerodynamic and inertial forces on the blades induces deformations that, in turn, alter the local aerodynamic load at different points in the blade's revolution. Capturing and understanding these deformations is essential for accurately modelling overall system performance.

2.1. Propeller-wing interference

Propeller-wing interference manifests through two primary effects: the modification of the wing's lift distribution due to the propwash, which introduces increased dynamic pressure and swirl, and the induced upwash on the rotor disk caused by the wing's lift. These interactions create a tightly coupled aerodynamic system where the performance of both elements is interdependent.

The behaviour of the wing's lift, while inherently complex, can be approximated as the sum of three contributions: the base lift distribution of the clean wing, the increased lift in the propwash region due to the increase in dynamic pressure, and the local variations in angle of attack induced by the swirl in the wake of the rotor's upgoing and downgoing blades.

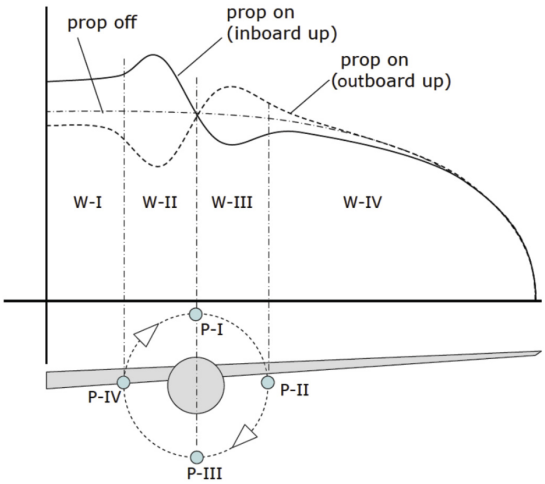

Figure 2.1: Wing lift distribution alteration induced by a tractor propeller (Alba et al., 2018).

At the rotor, three additional factors influence its inflow distribution: the lift distribution of the wing, its relative position with respect to the rotor, and the wing's angle of attack. Depending on the direction of rotation, the upgoing and downgoing blade regions effectively swap, as do the advancing and retreating blade regions relative to the inflow angle, altering the local aerodynamic loads on the rotor disk and on the wing.

Following the naming convention of Alba et al. (2018), four regions are defined on both the rotor and the wing, as illustrated in Figure 2.1.

For the wing sections W-I and W-IV, corresponding to the inboard and outboard out-of-wake regions, the lift distribution is similar in shape to that of the engine-off clean configuration and only slightly increased or decreased, depending on which wing section and on the propeller rotation direction.

In W-II, for a clockwise rotor, the blade swirl increases the local angle of attack, thereby increasing lift. The opposite is true in W-III where the downwash from the downgoing blade reduces the local α, thus decreasing lift.

The wing influences the inflow at the rotor disk with three key effects (Figure 2.2). The first is the geometrical mounting angle, which creates an α offset between the wing and the rotor. The second is the lift-induced upwash, which results in a vertical gradient depending on the wing relative location and the strength of its circulation. With sweep the lift-induced upwash also presents a horizontal component in its gradient. The third is the thickness effect, which results in an increase in static pressure and a decrease of axial velocity at the rotor plane, thus with a minimal change in inflow angle. The magnitude of this effect also depends, as for the lift-induced upwash, on the distance between the rotor and the wing.

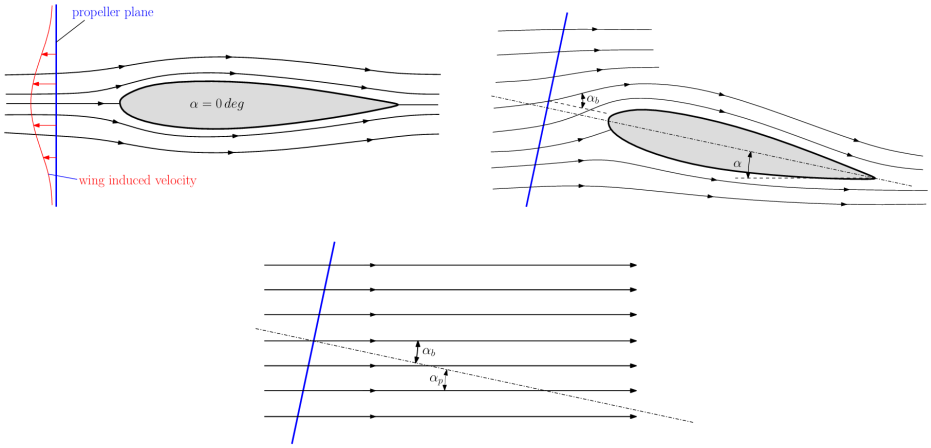

Figure 2.2: Wing interference at the propeller plane (Veldhuis et al., 2013).

Assuming the propeller is pitched relative to the flow, regions P-I and P-III experience only a spanwise component of flow, which has less impact compared to regions P-II and P-IV, as it does not directly impact the angle of attack of the blade (see Figure 2.1). For a positive angle of attack α, the downgoing blade in P-II experiences an increase in incidence due to the induced velocity combining with the relative in-plane velocity from the blade's rotation. The velocity triangle shown in Figure 2.3 demonstrates the effect. In contrast, in P-III, the induced velocity subtracts from the relative rotational velocity, reducing the incidence angle and, consequently, all aerodynamic loads on the blade in that region. The variation in angle of attack is more pronounced for the retreating blade than for the advancing one due the shape of the velocity triangle as shown in Figure 2.3. This asymmetry leads to a thrust increase at a constant advance ratio, provided that the power supplied to the rotor shaft is correspondingly increased.

The lift-induced upwash and the inflow caused by the propeller's geometrical angle of attack can affect the propeller loading similarly, depending on the relative position of the rotor disk to the wing (Veldhuis et al., 2013). The upwash is not uniformly distributed; however, the further the rotor disk is from the

wing's equivalent lifting line, the smaller the changes in velocity across the disk become due to the dependency of the flow field curvature on the distance from the vortex. In contrast, higher lift values and wing sweep angles can lead to increased asymmetry in the propeller loading, due to the different upwash strengths at the rotor which in turn change the effective incidence angle of the blades. This is simply due to the geometry change given by having a swept wing, with half of the rotor being closer to the leading edge for a tractor configuration and the other half further away. The upwash magnitude, which can be derived from the Biot-Savart law, depends inversely on the square of the distance and thus is greater where the wing is closer to the propeller.

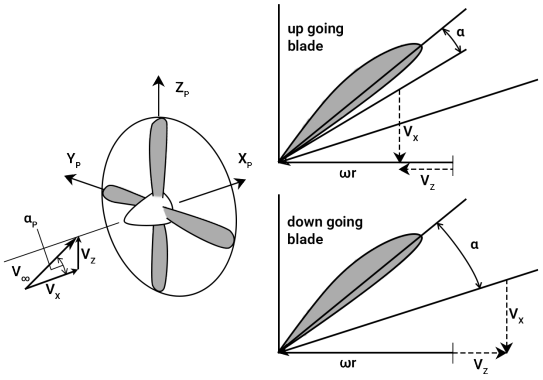

Figure 2.3: Velocity triangle for the upgoing and downgoing blade (Veldhuis, 2004).

Figure 2.4 shows that when the propeller's thrust axis is aligned with the quarter chord pivot line of a variable angle of attack symmetric airfoil, the effects of the inflow angle — whether due to the geometric angle of attack or the wing lift — are similar on the propeller's induced velocities.

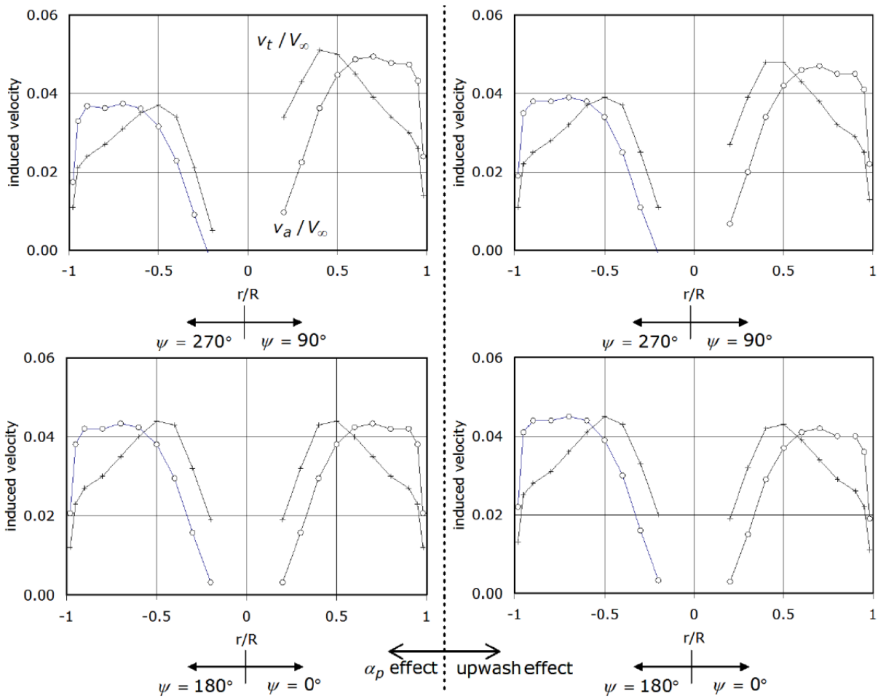

Figure 2.4: Tangential and axial velocity ratios for geometric angle of attack and lift induced upwash (Veldhuis et al., 2013).

This holds only for an unswept wing, because with wing sweep the asymmetry increases, causing the induced axial and tangential velocities to deviate from the simplified case based on the geometric angle of attack. High-lift devices such as slats and flaps increase the wing's lift by modifying the local pressure distribution, typically by altering the camber or effective angle of attack. This also shifts the centre of pressure forward, as lift becomes concentrated near the leading edge. Consequently, the lifting vortex strengthens, and the distance between the equivalent lifting line and the rotor decreases, intensifying wing-rotor interactions. The primary driver of this increased interaction is the change in lift magnitude rather than the lifting line's displacement.

2.2. In-plane propeller loads

To analyse the mechanism behind blade deformation the in-plane propeller loads - the dominant harmonic loads synchronized with rotor speed, must be first examined.

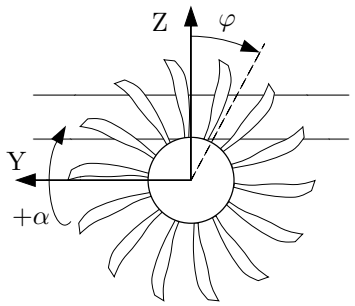

Figure 2.5: Model coordinate system from the REA54 test campaign.

Using the coordinate system shown in Figure 2.5, which differs from that of Sinnige et al. (2016) by accounting for the counterclockwise rotation of the rotor and the interchange of α and β, the upwash velocity w is in the positive z-direction for a positive α and can be expressed as:

$$w = V_\infty \cdot \sin\alpha$$

where α represents the uniform flow incidence angle relative to the thrust axis. The rotor disk is divided into two sectors: the advancing region ($0° < \varphi < 180°$), where the blade rotation is opposed to the induced upwash, and the retreating region ($180° < \varphi < 360°$), where instead the blade motion is aligned with the upwash.

The vertical lift component is given by the load imbalance in the two regions, with the advancing blades being subjected to a greater dynamic pressure and angle of attack, resulting in both more lift and drag. The resulting in-plane force for the advancing blades is directed up, in the positive Z direction. The exact opposite happens on the other side at the retreating blades, which, under less dynamic pressure and with a smaller incidence angle, result in a smaller in-plane force than when the thrust axis is aligned with the flow. The difference of the increase on one side and decrease on the other results in a vertical force that is the main component of the 1P load.

The horizontal component depends instead on the different loading at the blade azimuths close to $\varphi = 0°$ and to $\varphi = 180°$. This phase lag, with the shift in maximum loading from $\varphi = 90°, 270°$ is due to the unsteady aerodynamic effects which depend on the rotor reduced frequency. The local incidence and thus the load are reduced for $\varphi = 0°$ because it is in the wake of the highly loaded advancing blades, while at $\varphi = 180°$ the induced velocity from the retreating blade is not as significant. The load imbalance between the blades close to $\varphi = 0°$, less loaded than the ones at $\varphi = 180°$, results in a horizontal force directed in the positive y-direction.

The azimuth of maximum loading is therefore expected to occur slightly after the position where the advancing blades experience the highest tangential velocity—specifically around $\varphi = 90°$, where the blade's rotational velocity aligns with the freestream flow—resulting in increased aerodynamic forces. Thus, this peak loading is anticipated for azimuthal angles $\varphi > 90°$.

Test data from a previous campaign on the isolated APIAN propeller at various inflow angles and advance ratios validate the theory, showing periodic blade loading with a phase independent of the advance ratio. Due to the different rotor coordinate system used in Figure 2.6 (Sinnige et al., 2016), where $\varphi = 0°$ corresponds to $\varphi = 90°$ in the coordinate system of Figure 2.5, the maximum load at 30° in Figure 2.6 corresponds then to an azimuth of $\varphi = 120°$, occurring just after the blade experiences maximum upwash.

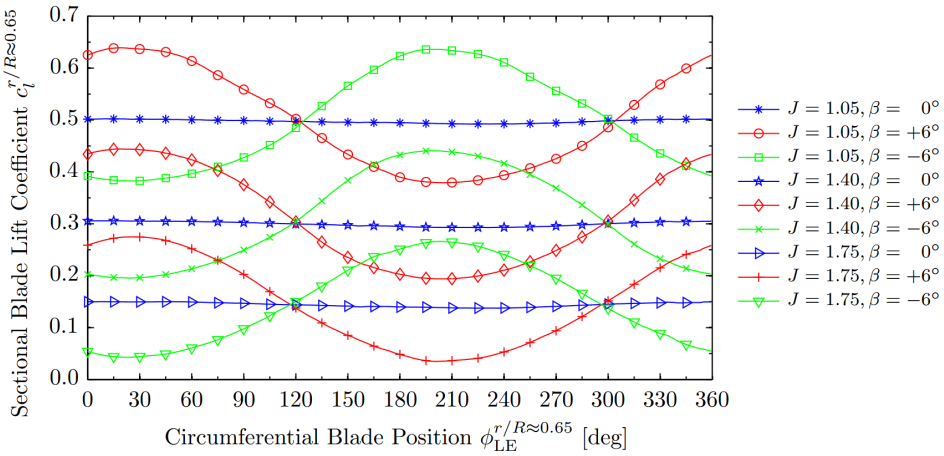

Figure 2.6: Effect of angular inflow on the propeller blade loading at r/R ≈ 0.65 - isolated configuration (Sinnige et al., 2016).

The maximum deformation is also expected near the location of maximum loading. Given that the REA54 and APIAN campaign rotors share similar solidity, tested Mach numbers, and dimensions, the maximum deformation can be expected at the same general azimuth. While the in-plane propeller forces—excluding those caused by the spinner and other non-lifting geometries—do not directly cause blade deformation around the rotor disk, their magnitude depends solely on the load imbalance, which is the common cause of both these forces and the deformation imbalance around the disk, the subject of this thesis. While given equal flight conditions the differences in chordlength between the APIAN and the tested rotor result in a considerable difference in propeller reduced frequency, the non-dimensional number which characterizes unsteady aerodynamic effects, the linear behaviour of the in-plane forces with the angle of attack is expected to remain valid. One other earlier test campaign ran with the same isolated APIAN propeller, tested at the transonic S1Ma wind tunnel in Modane in 1999, provides some insight on the magnitude of these in-plane forces at Ma = 0.2, as shown in Figure 2.7.

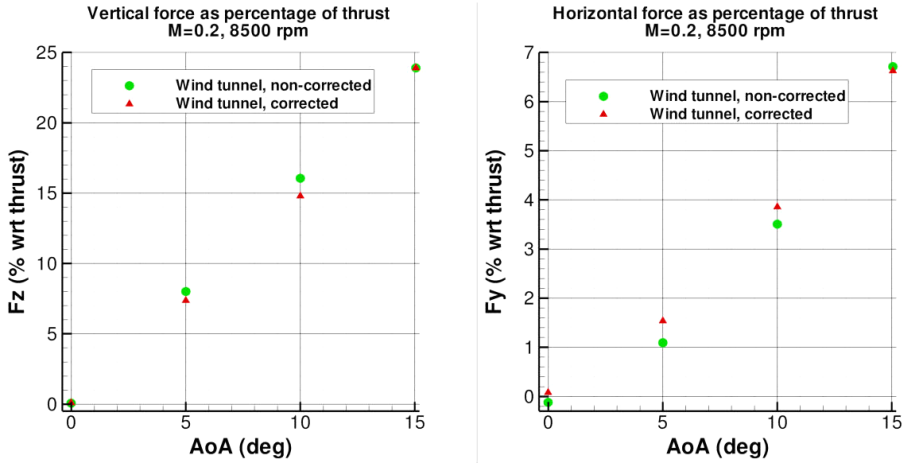

Figure 2.7: In-plane loads as percentage of thrust at Mach = 0.2 (Ortun et al., 2012).

The horizontal and vertical forces acting on the rotor, as measured by the RSB, result from an imbalance in the aerodynamic load distribution across the blades. This same load imbalance, which generates high F_Z values, is also responsible for the variations in deformation observed over one revolution.

Results are also available for Ma = 0.7, with a strongly increased dependency of the in-plane forces on the angle of attack.

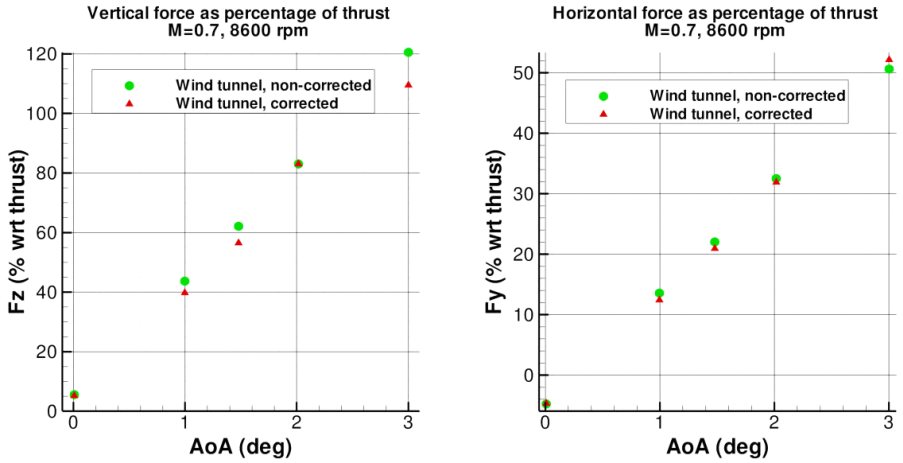

Figure 2.8: In-plane loads as percentage of thrust at Mach = 0.7 (Ortun et al., 2012).

As Mach number and dynamic pressure increase in higher-speed flight regimes, the influence of angle of attack on 1P forces generated by the rotor and spinner becomes more pronounced (Figure 2.8). In steady horizontal flight, the wing's lift remains constant by definition, but the rise in dynamic pressure reduces its angle of attack. Simultaneously, the increased velocity reduces circulation and enhances inflow at the rotor, resulting in a shallower velocity triangle.

Consequently, rotor loading becomes increasingly governed by compressibility effects and self-induced velocities, rather than by wing lift and angle of attack. The most critical condition occurs during take-off and landing, where multiple adverse factors lead to the highest non-uniformity in rotor inflow. Both conditions have a Ma $\approx$ 0.2, flaps are deployed to maximize lift and air density is at its highest. The circulation is therefore highest for take-off and landing over the whole flight profile, leading to the most upwash, while the freestream velocity remains low, resulting in the most significant variation in inflow angle across the rotor disk. Although landing may exhibit worse inflow distribution, the higher thrust required for take-off intensifies the impact of inflow variability on blade deformation — the primary focus of the analysis.

2.3. Principles and application of the Image Pattern Correlation Technique (IPCT)

IPCT measures the three-dimensional displacement field of a surface by subtracting its undeformed (cold-shape) from the deformed (hot-shape) state. It relies on stereographic triangulation using a dual-camera system, ensuring both cameras have full visibility of the object's patterned surface. Synchronized image pairs are captured and processed using camera matrices obtained from a prior calibration step. This calibration involves imaging a planar checkerboard target with a known grid pattern, allowing the camera matrices to be computed from the detected corners, under the assumption that they lie precisely on a flat grid with the edge length equal to 25mm. (Kirmse et al., 2021; Boden et al., 2023; Kirmse et al., 2016)

The reference measurement phase begins by capturing images of the cold-shape geometry, in this case, an unobstructed propeller blade surface in wind-off condition and without rotation. These images define a baseline surface model, accompanied by standard deviation metrics and a triangulation error field. Post-processing filters remove unreliable data points, typically near the leading or trailing edges or in

areas where dot markings have deteriorated due to abrasion or uneven contrast. The filtered data is then averaged to produce a single reference surface for all subsequent hot-shape measurements.

Hot-shape measurements follow a similar procedure but introduce two key changes: rotor synchronization to account for rotational motion and pulsed illumination to freeze movement. The reduced exposure time, even if coupled with increased flash power, necessitates higher camera gain, which amplifies image noise and contrast. Although this reduces the SNR (signal-to-Noise Ratio), spatial correlation algorithms remain effective due to the different scales of the pattern and the noise. Final displacement vectors are derived by aligning the hot and cold surfaces through a RBT (Rigid Body Transformation), which removes rigid motion artifacts by fixing the non-deformed root section as a reference. In order to align the two surfaces and eliminate any systematic error due to a rotation around the chord direction, which would introduce more bending, or the span direction, which would introduce twist, a reference area has to be used.

The RBT is determined by minimizing the residual displacement at the root of the hot shape, with the assumption that this region remains effectively undeformed. Selecting an appropriate reference area is crucial: if one side is too close to the tip, the assumption of negligible deformation becomes invalid, whereas a smaller reference area near the root may improve surface alignment at the cost of reduced leverage for correcting rotation about the root chord. This could introduce a displacement component that varies linearly with the distance from the root. The reference area covers approximately 90% of the chord, excluding regions near the leading and trailing edges where outliers tend to concentrate. Vertically, it spans 20% of the total blade height, starting from the side of the dot pattern closest to the root, with a similar margin left near the edges to avoid areas with higher outlier density.

The dot pattern is a critical component of IPCT, as its design and application directly influence measurement accuracy. The pattern is applied to the blade surfaces using a painted coating, which is subsequently sanded and finished with a thin layer of clearcoat to have a surface roughness comparable to the other blades. The pattern itself consists of three distinct types of elements (Figure 2.9), each serving a specific role in the analysis:

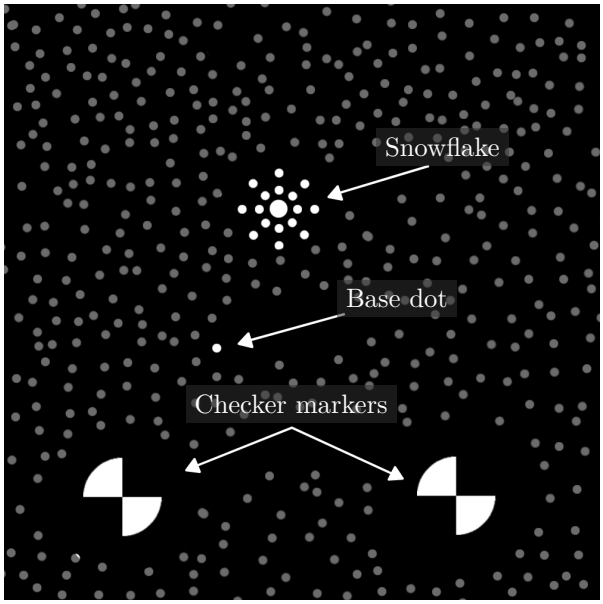

Figure 2.9: Elements of the painted pattern for IPCT.

Round checker markers: These markers are automatically detected by the IPCT software using their radius as a primary criterion, supplemented by a manual selection in the initial image pair. At least three common markers between the two cameras are required to define a RBT, which facilitates the initial alignment of masks and intermediate data files to compensate for blade motion, whether due to varying rotor azimuth positions or changes in sting configuration.

Snowflakes: These markers, so called because of their shape, consist of a central dot with twice the base diameter, surrounded by two concentric rings of eight smaller dots. Their distinct geometry allows for easy identification when manually selecting corresponding points between cold-shape and hot-shape images, while still conforming to the constraints of cross-correlation interrogation windows without introducing significant localised error.

Base dots: These constitute the majority of the pattern and serve as the primary reference for surface evaluation. Their dimensions are chosen such that they appear approximately three pixels in diameter in the recorded images. The dots are randomly and uniformly distributed across the blade surface to ensure comprehensive coverage and robust spatial correlation.

2.4. Deformation measurements

Two complementary techniques are available for measuring rotor deformations, each with distinct strengths and limitations: IPCT and strain gauges. IPCT provides full-field, non-intrusive measurements of blade deformation, capturing global bending and twisting, though it lacks the temporal resolution to resolve vibrational modes and cannot measure throughout the entire blade rotation. The technique can use either a painted pattern or a laser-projected one (Kirmse et al., 2016), with the significant advantage of being completely non-intrusive. This makes IPCT particularly valuable for measuring large-scale phenomena that would be challenging to instrument with strain gauges, such as jet engine fans (Kirmse et al., 2016), propellers (Lanari et al., 2013), or wings (Kirmse et al., 2021). Strain gauges complement this by offering high-resolution stress data, albeit only at discrete points, requiring deformation to be reconstructed from the measured stresses. Despite this limitation, strain gauges are essential for analysing vibrational modes and transient events, where precise timing is critical.

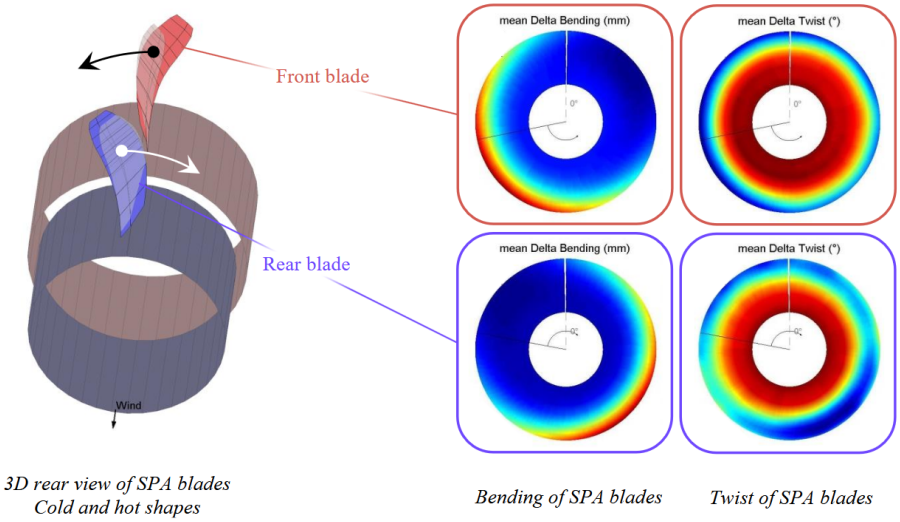

Figure 2.10: Deformation analysis of the PX-7 CROR (Geeraert & Stephan, 2015).

While the PX-7 engine tested in (Geeraert & Stephan, 2015) and simulated in (Mauffrey et al., 2015) is of the CROR kind, the bending distribution over the disk of the front blade follows the theoretical deformation of a simple rotor under angular inflow conditions. The point of maximum bending lies close to the location of highest aerodynamic loading, and the same is valid for the second set of counter-rotating blades with the opposite direction of rotation effectively mirroring the deformation across the vertical axis. The twist distribution is instead much less concentrated at one specific azimuth, suggesting that it is not a mere consequence of the bending but rather a different response of the system to the blade loading. Of course, twist plays a significant role in thrust generation, as it directly affects the aerodynamic performance of the blades. However, due to the measurement of the twist distribution being highly sensitive to mesh point outliers, inaccuracies arise, particularly near the blade tip. This makes the twist analysis much less reliable compared to bending, which is less affected by such variations. Furthermore, while bending data has been consistently available for several months,

the twist measurements only began to yield somewhat reliable results in the final week of writing this thesis. For these reasons, bending measurements were chosen over twist for a more accurate and stable analysis.

2.5. Research objectives

This research aims to experimentally analyse the impact of wing-induced inflow on propeller blade deformation in open rotor engines. Specifically, it investigates how lift-induced upwash, generated by the wing, modifies the flow field at the rotor, leading to changes in the blade's aerodynamic loading and structural response. To achieve this, the study employs IPCT to capture full-field blade deformation patterns under different operating conditions. The research also evaluates the effectiveness of using mean lift-induced inflow models to predict the rotor's response, with a focus on comparing wing-on and wing-off scenarios. By assessing the accuracy of corrections that account for the induced upwash and the change in angle of attack at the rotor, the study aims to improve the understanding of rotor performance in the presence of wing effects and provide insights into more accurate predictions for open rotor engine design.

A central aspect of this study is understanding the influence of spatial inflow non-uniformity on the rotor deformation behaviour, as well as determining how variations in inflow distribution affect the accuracy and applicability of the inflow angle correction methodologies. The findings will contribute to improving predictive models for rotor deformation, providing a more detailed understanding of fluid-structure interaction effects in open rotor configurations.

To achieve this goal, key research questions were posed, forming the foundation of this thesis:

1. *How does the lift-induced upwash from a downstream wing affect the rotor and stator deformation of an upstream engine?*
2. *To what extent does the inflow angle correction, derived from lift-induced upwash models, enable wing-on data to correlate with wing-off deformation measurements?*
3. *How does the inflow distribution caused by sweep affect the deformation dynamics of the rotor and the reliability of the inflow angle correction methods?*

3

Experimental setup

3.1. Wind tunnel setup

The experimental campaign was conducted at the Large Low-Speed Facility (LLF) of the German-Dutch Wind Tunnels (DNW), a closed-circuit wind tunnel featuring an open test section with dimensions of 6x8 m. The facility operates within a Mach number range of 0.01 to 0.2, reaching a maximum flow velocity of 68 m/s. For a reference length of 1 m, it is capable of achieving a Reynolds number of up to 3.8×10^6. The LLF is characterised by high flow quality, with turbulence intensities of 0.02% in the longitudinal direction and 0.04% in the lateral direction. Additionally, it maintains a high degree of flow uniformity, with a pressure coefficient variation of $\Delta C_P = 0.001$, minimal flow angularity below 0.06°, and temperature uniformity within ±0.2°C (German-Dutch Wind Tunnels (DNW), 2025).

The model consists of a central nacelle section housing both the pneumatic motor drive and the RSB for the rotor. Extending from its sides, two lateral booms support the wing structure, enabling adjustments in both longitudinal and vertical positions. Additionally, the sweep angle could be modified to simulate either a port or starboard engine configuration.

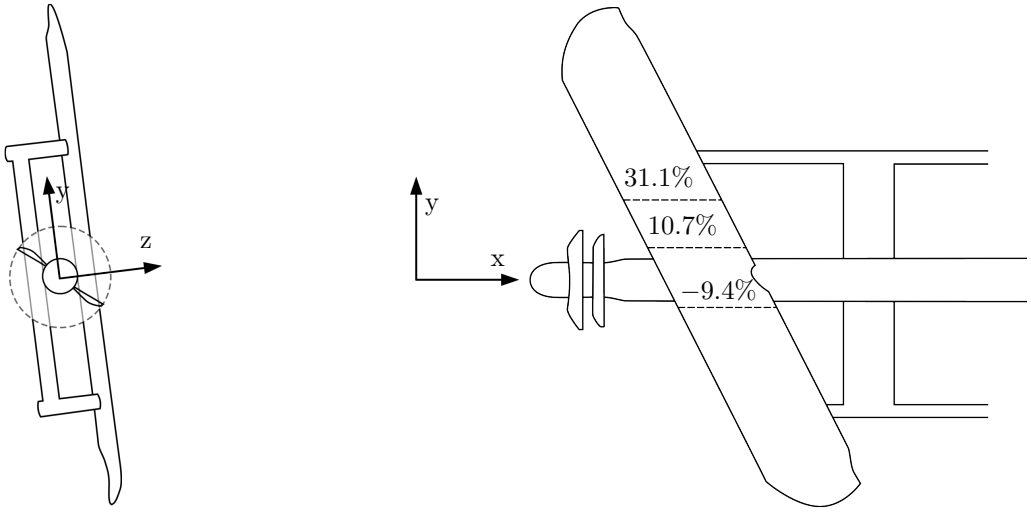

Figure 3.1: Model coordinate system. Pressure sensors located on the dashed lines of the right image with the relative η position.

However, none of these three possible geometric adjustments — namely the horizontal and vertical

distances between the nacelle and wing and the sweep angle — were ultimately implemented during testing due to time constraints and in-situ decisions made by the Airbus team, which managed the common test phase that generated the data used in this thesis. The specific dimensions for the tested configuration are given in Table 3.1.

Table 3.1: Wing and Rotor Geometric Parameters

Component	Dimension
Rotor diameter	1 D
Rotor centre to quarter chord horizontal distance	0.94 D
Rotor centre to quarter chord vertical distance	0.24 D
Wing chord length	0.94 D
Wingspan	5.3 D
Wing LE and TE sweep	27°

The model is located at the wind tunnel centerline and mounted on the sting, but it is rotated around its longitudinal direction by 83°. This meant that the sideslip movement of the sting corresponded to the angle of attack of the model and vice versa. One factor that was of importance to the camera setup was the dependency of the longitudinal rotor position from the angle of attack due to the sting requirement to keep the model always on the centerline.

3.2. Propeller and wing specifications

The originally planned configuration changes allowed for two vertical and four longitudinal wing positions, with the possibility of changing the sweep angle. Different kinds of leading edge geometries were also used. The wing and slats housed pressure ports at three different span locations η, defined as -1 at the downstream wingtip and 1 at the upstream one, with one in the downwash of the rotor at $\eta = -9.4\%$, one in its upwash at $\eta = 10.7\%$ and the third set outside of the rotor slipstream at $\eta = 31.1\%$. Their location is shown in Figure 3.1 as the dashed lines in the view of the top of the wing. The lift data obtained from the integration of the pressure distribution is later used to model the lift induced upwash at the rotor disk.

At the front of the model is present the static nose with transition dots, followed by the rotor, which consisted of 14 carbon composite blades with continuously variable rotor pitch. Behind it is the stator, featuring the same pitch regulation mechanism for continuous adjustment. Unlike the rotor, the stator blades were made of steel, providing a much higher stiffness.

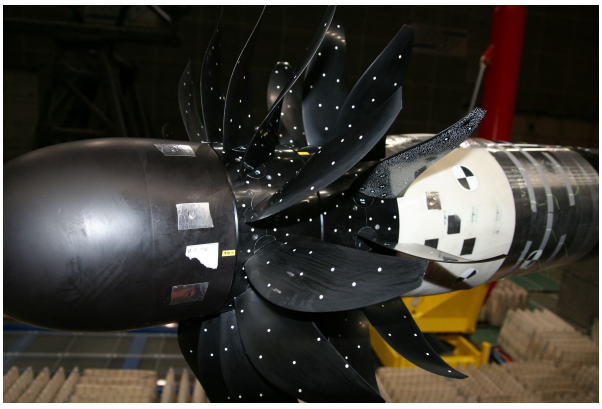

Figure 3.2: Engine during the assembly phase with both the IPCT pattern and the NLR dot markers for blade alignment shown. Both the hub transition strips and the wing are absent.

Both rotor and stator could be removed and substituted by a simple blade-less ring to simulate only the rotor or the clean airframe configurations. Due to the increased stiffness paired with the reduced

aerodynamic and rotational loading, the stator blades were not expected to have deformations of comparable magnitude with respect to the rotor. While the rotor had 14 blades the stator only had 13, with equal spacing, with the missing blade being located where the engine pylon would be on a full scale aircraft. All the measurements were taken on three unique blades, one for the rotor that was measured twice at opposite azimuths by both camera systems (Figure 3.3), and two opposite stator blades, one for each pair of cameras.

All the round white dots present on the rotor, stator and ring mount surfaces as shown in Figure 3.2 were necessary for the blade angle alignment tool developed by NLR and were not part of the IPCT pattern. As the dots were present both on the suction and pressure side of the rotor they were redundant, which made it possible to manually cover the ones visible from the front with a black whiteboard marker in one of the tries for the stator measurements later shown in Appendix A.

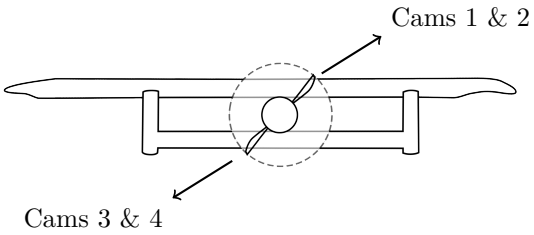

Figure 3.3: Location at which the rotor and stator blades are imaged by the two camera groups.

3.3. Cameras and flashes

The setup consists of four cameras, paired in two stereo groups located respectively on the left and right side of the inlet nozzle (Figure 3.4). Each stereo group is responsible for the measurement of the rotor blade in one portion of the propeller disk and of a single stator blade. The cameras are four *AVT Bonito PRO X-2620*, equipped with a 26MP black and white sensor with an electronic global shutter (Table 3.2).

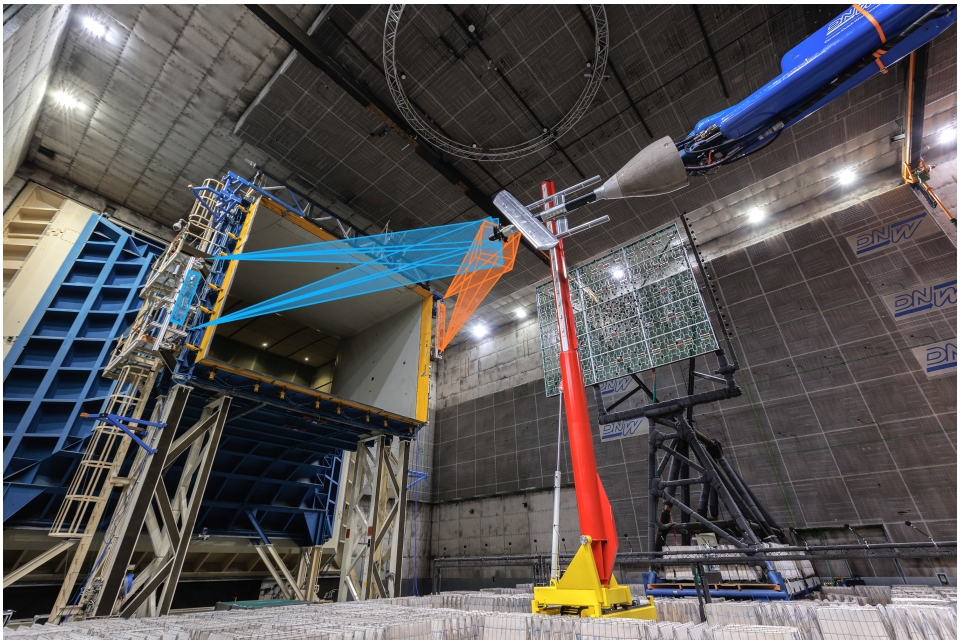

Figure 3.4: Field of view of the two camera pairs, C12 (blue) and C34 (orange). The flashes are highlighted between the cameras.

Given the APS-H sensor size and the distance of the nozzle to the propeller of 9m, the focal length

required was in the order of 200mm. The most suitable lens of which there were at least four available was the Zeiss Sonnar 180mm f/2.8 which was then chosen for the test campaign.

Table 3.2: Camera specifications (Allied Vision, 2024).

Interface	CoaXPress (CXP-6) 4 DIN
Resolution	5120 (H) × 5120 (V)
Sensor	ON Semi PYTHON 25K
Sensor type	CMOS
Sensor size	Type APS-H
Pixel size	4.5 µm × 4.5 µm
Shutter mode	GS (Global shutter)
Max. frame rate at full resolution	79.7 fps
ADC	10 Bit

The camera requirements are linked to the ones of the dot pattern, because both the magnification factor and the physical dot size control the relative dimension of the dots on the images, which for best results should be close to 3px in diameter.

From the thin lens equation

$$\frac{1}{f} = \frac{1}{d_i} + \frac{1}{d_0} \tag{3.1}$$

and given that $d_0 >> f$ we can approximate $f \approx d_i$. This results in a magnification ratio of

$$M = \frac{d_i}{d_0} \approx \frac{f}{d_0} = \frac{0.18m}{9m} = 0.020 \tag{3.2}$$

Considering the pixel size of 4.5 µm and the magnification ratio M in order to achieve a diameter of 3 pixels the dot diameter has to be

$$d_{dot} = \frac{3px \cdot 4.5\mu m/px}{M} \approx 0.6mm \tag{3.3}$$

which is what is used on the blades for the base dots. It's assumed that a camera is diffraction limited when the Airy disk is larger than 2.5 times the pixel size, we can therefore calculate the limiting aperture.

$$d_{diff} = 2.44\lambda(1+M)f \tag{3.4}$$

Which results in a maximum aperture of

$$f = \frac{d_{diff}}{2.44\lambda(1+M)} = \frac{2.5px_{size}}{2.44\lambda(1+M)} \approx \frac{4.5\mu m}{500nm \cdot 1.020} = 8.82 \rightarrow f/8 \tag{3.5}$$

The other aperture limit is given by the movement range of the model and the required depth of field to cover it. In order to always keep the model at the wind tunnel centerline the sting is designed with two hinge points, one downstream at its base and one towards the model. This results in a longitudinal translation of the rotor disk for increasing α, but at the same time the rotation by α moves the lower blades (at $\varphi = 180°$) towards the right stereo group of C34 and the upper blades (at $\varphi = 0°$) away from the left cameras of C12. This means that a fixed focus point, while mandatory due to the camera calibration being dependent on always having the same focus, is not optimal as the focus points shifts considerably. The result of this is that the depth of field of both camera groups has to always cover the complete movement range, at the expense of image brightness, as shown in Figure 3.5

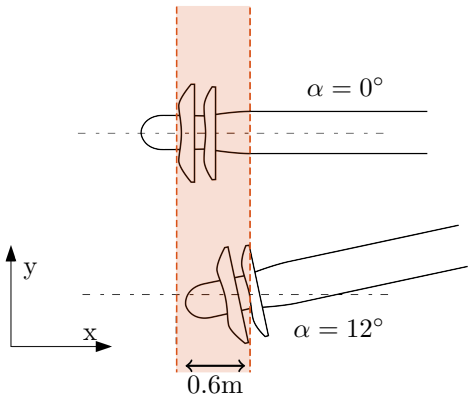

Figure 3.5: Downstream shift of the rotor resulting from α change. Necessary depth of field shown in orange.

The necessary depth of field was given by the maximum downstream movement of the rotor blade over the complete range of angles of attack, from 0° to 12°. The subject distance of 9m made it necessary to use 180mm focal length lenses and from there, using a value for the circle of confusion c of 0.025mm, the aperture was found from Equation 3.6 equal to f/5.6 in order to cover the 0.6m of rotor movement.

$$N = \frac{DOF \cdot f^2}{2d_0^2 coc} = \frac{0.6m \cdot (180mm)^2}{2 \cdot (9m)^2 \cdot 0.025mm} \approx f/5.6 \tag{3.6}$$

All four cameras and flashes are aligned and focused on the model at the wind tunnel centerline, with the angle of attack set to the midpoint of the tested range. This position, corresponding to the propeller's halfway longitudinal movement, allows the entire depth of field to be used, avoiding the need to close the aperture further and risk reducing image brightness.

The distance of the cameras to the propeller disk is on average of 9m, with a depth of field of 600mm and a field of view of 1x1m at the rotor plane. Each stereo group is independently triggered via a dedicated cable, ensuring precise synchronization with the corresponding flashes. The flashes are positioned on the same support beam as their respective stereo groups and only fire once per revolution. Not using both flash groups at the same time for a given blade measurement might seem like a loss of half of the illuminations, but preliminary tests revealed that flashes on the opposite side do not contribute to increased illumination. Instead, they introduce unwanted reflections due to the highly reflective surface of the blade, which is painted with a thin layer of clearcoat. These reflections manifest as overexposed and clipped regions in the image, significantly degrading the quality of the results by obscuring the dot pattern and locally rendering the cross-correlation impossible. To obtain glare-free images, the setup was designed to exclude opposite-side flashes, prioritizing direct and controlled illumination from the same side as the cameras. This configuration trades a slightly lower SNR due to increased sensor gain with a more uniform pattern illumination, which in the end gives results of much higher quality.

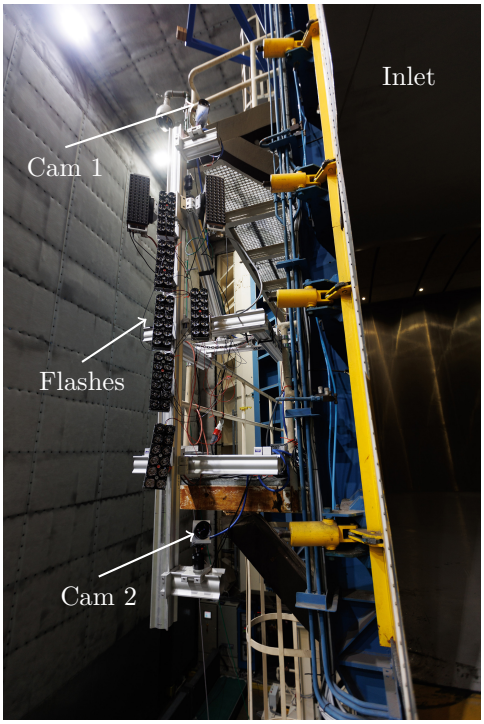

Figure 3.6: LEDs and cameras assembly on the lower left side of the inlet nozzle.

The two illumination groups are setup in the same way and are composed by two different kinds of flash lamps as visible in Figure 3.6. The two on top of the beam have integrated software and multiple I/O ports for the management of other units. Both of them are connected to the camera computer located down at ground level via Ethernet (Figure 3.7). Their software manages all safety aspects and all controls of brightness, exposure time and frequency limits. One of them is set as master and its TTL output controls all the other flashes in the group, allowing them to be synchronized.

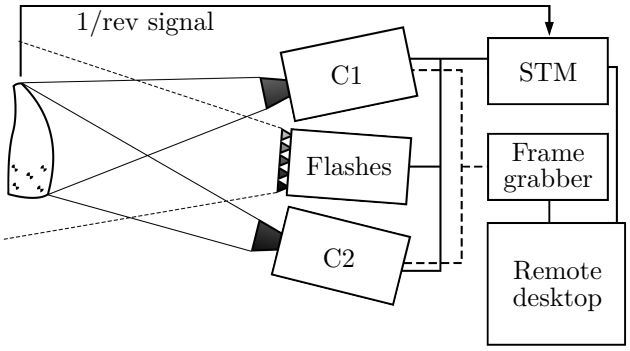

Figure 3.7: Hardware setup for one camera pair.

The remaining six LEDs mounted on the beam were developed internally by DLR and are powered by an 80V supply line with a single trigger cable. All six LEDs are connected in parallel and are hardware-only devices without any embedded software, relying solely on the trigger signal provided by the master LED positioned at the top.

The main concern regarding the flashes is then an exposure time which grants blur-free images while having a brightness that is good enough for the cross correlation to work near the root, where the shadows are more intense. On the camera side the aperture is as wide as allowed by the depth of field when set to f/5.6, and the sensor gain is also as high as the software allows for. The LEDs have a power

curve as shown in Figure 3.8, with the maximum current decreasing for an increasing exposure time, while the total amount of light output also increases with the time. This means that the maximum energy output is obtained for a lower current, with the limit being dependent on the maximum exposure duration which is set by the lamps rather than by the cameras, which keeps the shutter open for $100\mu s$.

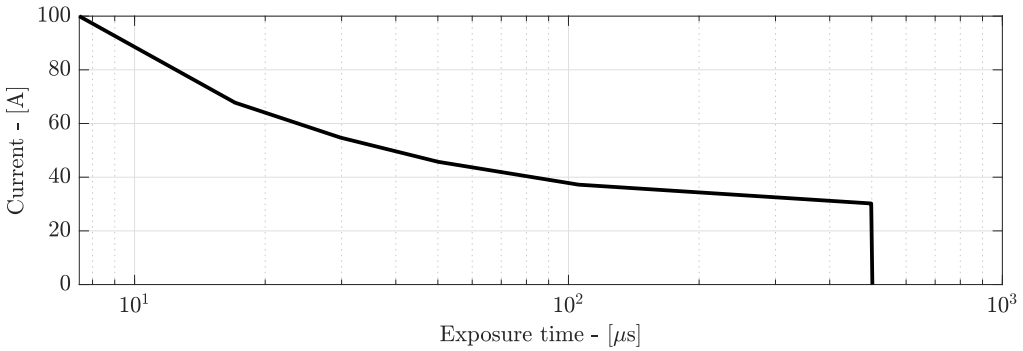

Figure 3.8: Power curve of the HardSoft LEDs in high power pulse mode.

The maximum exposure time is calculated as in Equation 3.7, using the worst case parameters for the *rpm* and a maximum allowable shift of 0.5px.

$$t = \frac{0.5\,\text{px} \cdot 4.5\,\mu\text{m/px}}{M} \cdot \frac{60}{7071\,\text{rpm}} \cdot \frac{2}{D} = 3\,\mu\text{s} \tag{3.7}$$

The maximum allowable shift of 0.5px at the blade tip corresponds to approximately one-sixth of the dot diameter. This remains within acceptable limits, as the slight blurring of the pattern preserves its shape on both cameras, ensuring the validity and accuracy of the cross-correlation method.

3.4. Triggering and synchronization

The computer responsible for the correct triggering of all the images, the STM (Standalone Trigger Module), uses the 1/rev trigger signal coming from an optical sensor in the rotor of the model to operate. The signal goes high when the eight blade of the rotor passes by the top position. This means that the STM has its reference shifted by $\approx 257°$, as the IPCT blade with the pattern is the 12th out of 14. All the azimuth angles have been shifted to follow the same reference as the one given in (Veldhuis et al., 2013), so clockwise with $\varphi = 0°$ on the top position close to the wing.

The 1/rev is a TTL signal in the range 0-5V and the STM takes the rising edge as its reference point; from there the angular velocity and revolution time are calculated. This allows the STM to trigger the cameras consistently at the same relative rotor azimuth. In the matrix the points with the lowest advance ratio have a period of $23\mu s$ per degree of rotation, so an accurate triggering of the imaging system is mandatory in order to have images with the same field of view. This is mainly true for the stator imaging, where one degree of rotor movement is approximately equal to 3mm of the chordlength at 50% r/R being covered by the rotor, but also for the rotor where the trailing edge may fall either in the shadow of the leading edge of the following blade or even be completely occluded by it. The approximate usable range in azimuth for rotor images is in the order of 5-10° for a fixed model α. The issue that limits the range is the presence of stray reflections which overexpose the pattern, and considering that their location is also dependent on rotor pitch and model α the optimal azimuth angle for the imaging has to come from experimentation rather than from geometrical considerations made with the CAD model.

The azimuth angle for rotor imaging was chosen at a model α of 6°, midway through the tested α range and between the two usable rotor azimuths, to minimise the aforementioned issues.

The stator imaging instead was influenced by every other variable, so it was not possible to choose a single azimuth angle at which to take the images and keep it constant for the whole test. It was then chosen to proceed with the method that used multiple exposures and digital image merging, as that

had worked in the lab setting before the test, and because it allowed to shoot ”blindly” and record multiple images at different relative azimuths, solving therefore the issue of the stator visibility. To keep the acquisition time short and to avoid taking too much data it was decided to take four equally spaced images for one rotor pass. Considering the 14 rotor blades this meant 4 images in the span of approximately 25°, which in practice was implemented as a spacing of 6.5° between the different images. This part is discussed much more in detail later in Appendix A.

The measurement sequence was then set up to take a total of 250 images per stereo group, with a data usage of 6.1GB per sequence per camera, divided into 100 rotor images at the optimum azimuth for the rotor imaging, then three sets of 50 images each, with a shift equal the quarter blade angle of 6.5° between them. The first 100 images are only used together for the surface measurement of the rotor blade, but the second half is used in the processing for the stator measurement as well, so the 50 stator images are obtained from merging 4 sets of 50 partial images. Due to the model shaking all images had to be aligned using the extra markers previously placed on the wing before any merging could take place.

One issue with the maximum frequency at a given current of the LEDs required to set a *skip trigger* equal to 3 in the STM code, which ignored three trigger signals out of four, reducing the effective firing frequency of the LEDs by 75%. The two limits that needed to be avoided were the maximum sequence time of 30 seconds, which was the time at which one datapoint was recorded by the wind tunnel, and the maximum firing frequency of the LEDs, which if exceeded would produce black images, as the cameras would shoot regardless of the presence of illumination.

3.5. Calibration

In order to find the relative position of the two cameras it is necessary to do a calibration using a checkerboard flatplate. All four cameras capture the plate at the same time as they are pointed to the same general area of the propeller disk, but the two stereo systems are independent from each other.

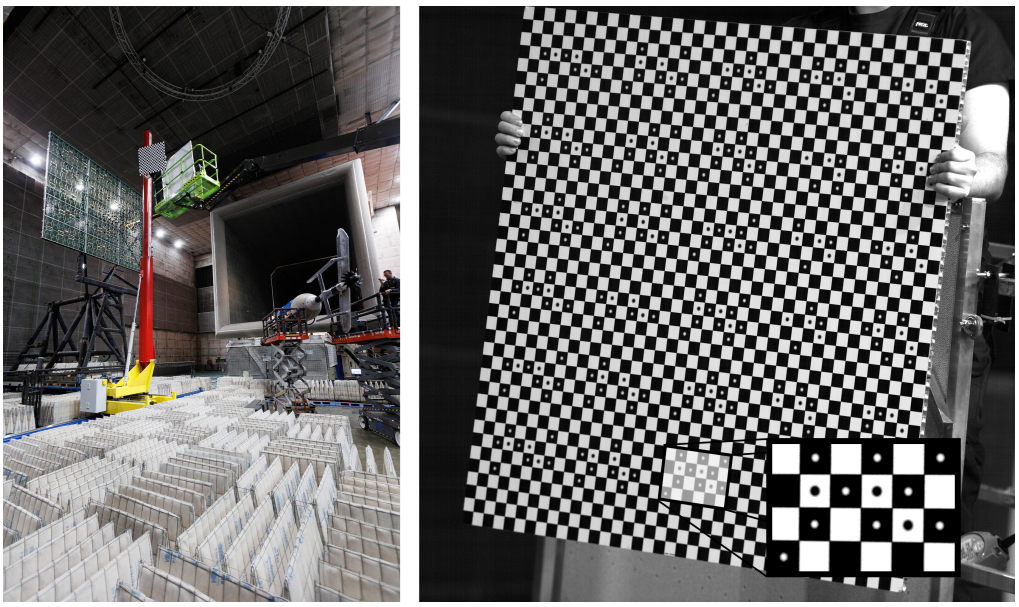

Figure 3.9: Calibration plate position (left) and as viewed from Camera 1 (right), with detail of the unique dot pattern.

The calibration plate is manually positioned at the rotor disk location along the wind tunnel centerline, aligning with the rotor's expected position for $\alpha = 0°$. It is then systematically shifted left/right and up/down within the camera reference frame to cover the test volume in which the rotor blades are located during the test.

The unique dot pattern, shown in the lower right of Figure 3.9, is necessary to uniquely correlate the two calibration images from each stereo group. To enhance calibration accuracy, the plate is further

translated along the wind tunnel x-axis (upstream and downstream) and rotated by 15° and 30° around the y- and z-axes of the wind tunnel coordinate system. These adjustments help mitigate potential calibration errors arising from slight depth-of-field variations within each stereo group.

To verify measurement quality and detect any camera position shifts that could compromise subsequent measurements, a flat plate is employed. This plate features the same pattern as the rotor and stator blades, consisting of random dots, snowflakes, and round checkerboard markers (Figure 3.10).

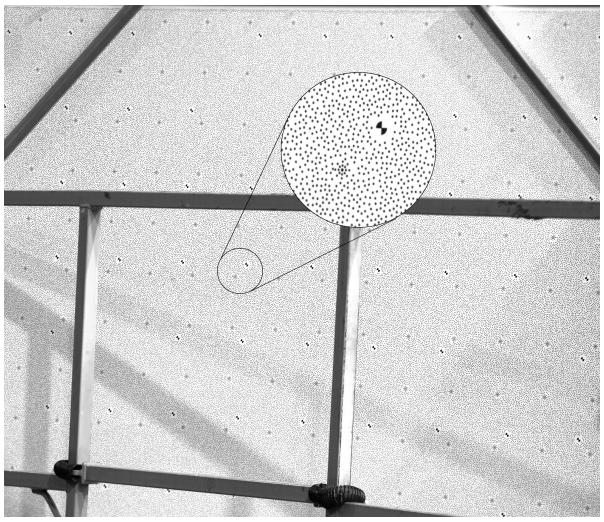

Figure 3.10: Test flat plate inside the boom-lift basket, as viewed from Camera 1, with a detail of the dot pattern.

The flat plate images are then evaluated to find the accuracy of the camera systems by the average triangulation error. Any clear directional gradient in the distribution of the triangulation error over the plate would indicate a movement in either of the cameras, even then due to the long focal length the gradient would not be as evident and would probably appear as a constant increase in error for the whole plate.

The two image pairs, one for each stereo group, are masked to remove the outline of the boom-lift basket which is in front of the plate. While for the calibration the unobstructed view was necessary, this measurement does not require it and given the size and weight of the plate the images were captured with the plate in a safer position stored inside the basket.

The resulting measurement, shown in Figure 3.11 for the C12 camera system, gives a general impression of the distribution of the triangulation error in the space which will be occupied by the rotor during testing. The triangulation error needs to be kept under 1px, which corresponds to the 0.1mm accuracy of the IPCT setup. Multiple measurements are done with the flatplate at an angle and at different downstream positions covering 1m, in order to verify the measurement accuracy around the position occupied by the rotor for different angles of attack, as shown in Figure 3.5.

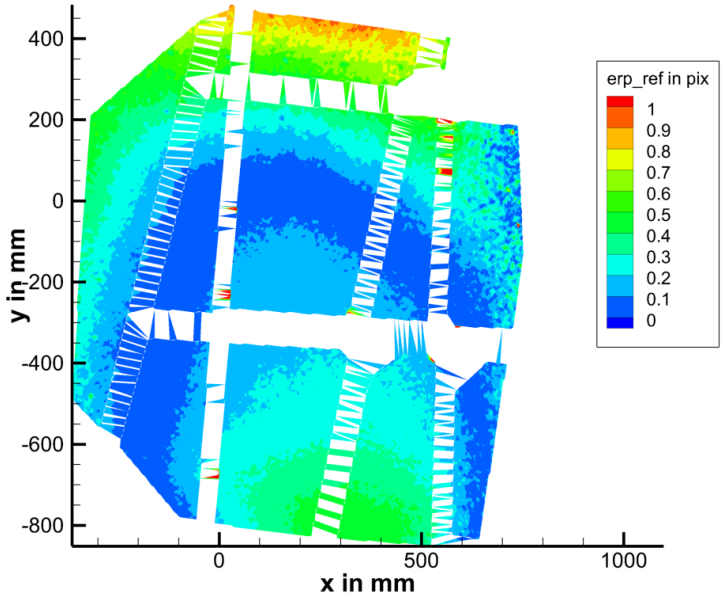

Figure 3.11: Triangulation error E_t distribution on the test flatplate.

3.6. Reference Measurements

The reference set of images is captured to establish the cold shape of the blade, serving as the baseline for displacement calculations in all subsequent deformed blade measurements. These images are acquired in rapid succession while the rotor blades remain stationary. Manual acquisition ensures unobstructed views from both cameras, with the rotor being adjusted by hand until the azimuth satisfying all criteria is found. Due to safety regulations regarding LED use, ambient light is employed instead of controlled illumination, necessitating the consideration of reflections from various light sources, such as overhead lamps, during the reference measurement.

The only movement observed during the reference capture is the oscillation of the sting, resulting from hysteresis in the hydraulic actuators, which produces a small elliptical motion. This minimal movement does not influence exposure time, as it is slow enough to prevent motion blur, but it causes a slight shift in the rotor position of at most 20 pixels.

To establish a consistent coordinate system for deformation analysis, a sequence of RBTs is applied. The first one move the surface from the reference measurement to the CAD geometry and is determined manually. The second one instead is needed to align the blade to the x-z plane and ensure that the primary bending mode aligns with the y-direction.

The reference dataset provides a surface with an associated mean triangulation error and its standard deviation. A threshold of 1px is applied to remove points with an excessive triangulation error, ensuring only accurate data remains. The mean triangulation error is respectively equal to 0.13px for C12 and to 0.33px for C34. These values correspond to an absolute error, defined as the value of the smallest distance between the two projection lines corresponding to a given point, of 0.21mm and 0.47mm. What matters is not the absolute displacement, as that is later corrected via a RBT, but the gradient which results in a erroneous component in the deformation. The deviation from the mean error is the accuracy of the measurement, as is approximately 0.1mm. The filtered surfaces are then averaged, producing a reliable reference measurement. Since this reference serves as the foundation for all subsequent data points, achieving the highest possible accuracy is essential.

For the rotor reference, achieving uniform illumination without stray reflections or shadows is relatively straightforward due to the rotor blades not overlapping too much. However, obtaining a clear reference for the stator required a different approach, as no stator blade is ever completely visible from both

cameras at the same time. Instead of disassembling the rotor, which would have caused significant delays to the already constrained wind tunnel schedule, the stator reference images were captured through a series of partial images. These images had to be first aligned due to the sting movement and then combined to construct a set of images with the complete stator surface visible, with the process being further discussed in Appendix A. The evaluation process is then the same as for the rotor.

Initially, it was assumed that the sting supporting the rotor was perfectly stable in space. However, given the stringent accuracy requirements of $0.15mm \approx 0.5px$, even minor positional shifts had to be accounted for. To ensure proper alignment of the partial stator images, additional markers were placed on the wing and fuselage. These markers were used solely for the initial alignment of the images, ensuring that any positional variations in the sting or camera setup did not introduce errors into the final reference frame.

4

Upwash and deformation modelling

This chapter calculates the effective inflow at the rotor using lifting-line theory, which relies on a circulation distribution derived from the three available sectional lift coefficients on the wing. The influence of wing sweep and propeller rotation on the inflow is also discussed. The spanwise deformation is presented, and the area over which the bending is averaged for further analysis is selected.

4.1. Inflow

The lift-induced upwash at the rotor disk is modelled using a simple lifting-line approach, based on a spanwise circulation distribution interpolated from pressure data measured at three wing sections.

4.1.1. Lift distribution

The lift data is provided by Airbus as three c_L values, each corresponding to a set of pressure sensors. These sensors are positioned with one outside and two inside the rotor wake, where the dynamic pressure is increased, and the effects of rotor upwash and downwash are present.

The lift distribution is reconstructed by interpolating six points: three from experimental measurements at the sensor locations and three based on assumptions. Zero lift is assumed at both wingtips, while an additional point is placed symmetrically relative to the out-of-wake pressure sensor set. This approach relies on the assumption that the lift distribution outside the propeller wake is symmetric. Due to the wing sweep the assumption of symmetric lift distribution is only an approximation (Cheng, 1978), but it remains a reasonable simplification for the present analysis.

The circulation distribution is then obtained by first converting from c_L to Γ with

$$\Gamma = \frac{1}{2} V_\infty \cdot c_L \cdot c \tag{4.1}$$

and then by fitting a cubic spline over the points.

Other errors which cannot be reduced further are the position in which the lifting line is located that is constant at a quarter chord on the wing. The presence of flaps and slats modifies the wing centre of pressure and therefore the line on which the circulation should be applied in the code. In all the following figures the circulation is shown normalized against a $\max(\Gamma)$ value, which is obtained from the maximum predicted lift in engine off configuration, obtained from the spline interpolation of the outer four points, excluding the two measured c_L values inside the propeller slipstream. Due to this it is possible that the value of $\Gamma/\max(\Gamma)$ is greater than one, but that is only the case for some polars in the region behind the upgoing blade, affected by its upwash.

4.1.2. Induced Velocity

The induced velocity at the rotor disk is modelled using a lifting line representation that accounts for bound vortices but neglects trailing ones. For any point $\mathbf{r}$ in space, the induced velocity is given by:

$$\mathbf{V}(\mathbf{r}) = \frac{\Gamma}{4\pi} \int_{-b/2}^{b/2} \frac{\mathbf{dl}' \times (\mathbf{r} - \mathbf{r}')}{\|\mathbf{r} - \mathbf{r}'\|^3}, \tag{4.2}$$

where Γ is the circulation obtained by interpolating the lift distribution, $\mathbf{dl}'$ is the infinitesimal vector along the wing's quarter chord line, assumed to be a straight line for a swept rectangular planform, $\mathbf{r}$' is the position on the lifting line and $\mathbf{r}$ is the test point at which the induced velocity is evaluated.

4.1.3. Inflow Components

The inflow incidence angle field at the rotor disk results from the combination of the freestream velocity and the induced velocity. This resulting inflow field, called α_{eff}, is broken down into several components: the geometric angle of attack, α_{G}, the uniform increase in inflow angle with value taken at the rotor centre, α_{C}, the vertical gradient component, α_{Vgrad}, and the nonlinear component, $\alpha_{\text{Nonlinear}}$, which represents the remaining part of the flow not captured by the other ones. These are shown in Figure 4.1.

The geometric angle of attack, α_{G}, defines the baseline inflow direction and is the only factor present in the isolated propeller testing. The correction term, α_{C}, accounts for the increase in inflow angle at the rotor centre, aligning wing-on data with isolated propeller data for bending analysis. The vertical gradient, α_{Vgrad}, represents the variation in inflow angle across the rotor disk, interpolated linearly between the lowest and highest points of the rotor, respectively from $\varphi = 180°$ to $0°$ at $r/R = 1$. This component introduces a $180°$ periodic effect on the deformation, and thus cannot be resolved by the stereo camera system due to aliasing.

The final component, $\alpha_{\text{Nonlinear}}$, represents the residual effect of the effective inflow angle, α_{eff}, minus the contributions from α_{G}, α_{C}, and α_{Vgrad}. This component captures the non-linear effects that remain unaccounted for in the linear model, contributing to higher-order periodic effects on rotor bending. Although these effects are more challenging to predict, their magnitude is significantly lower than that of the primary upwash components, making it possible to quantify them by analysing phase changes in rotor deformation.

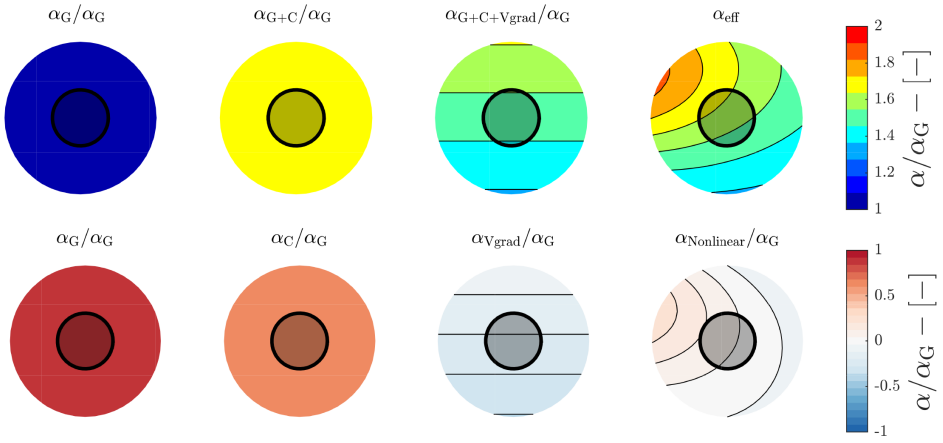

Figure 4.1: Inflow components normalised by the geometric angle of attack α_{G}, presented additively (top row) and individually (bottom row).

This subdivision of the inflow components allows for a more detailed analysis of how each part of the inflow influences the deformation of the rotor blades. The angle correction α_{C} explains the average bending of the rotor, while the vertical gradient α_{Vgrad} divides the rotor loading into four equal quadrants in the simplest non-uniform case, producing a sinusoidal loading variation with a period of $\varphi = 180°$. Assuming a sufficiently small inflow gradient, this pattern occurs without any measurable phase rotation, as the changes are symmetric and opposed in pairs.

4.1.4. Wing geometrical influence

The geometry of the wing strongly affects the induced angle of attack across the rotor disk, primarily due to the wing's sweep and the asymmetric lift distribution. This non-uniformity becomes significant, especially at high lift and dynamic pressure, where the variation in inflow angle between the downgoing and upgoing blades can reach up to one third of the mean incidence angle increase caused by the lift-induced upwash. The measurement azimuths, offset by approximately 180°, make it difficult to account for this non-uniformity in a straightforward manner.

The primary factor influencing the inflow non-uniformity on the rotor is the wing sweep. The point on the leading edge of the wing closest to the rotor is located towards the starboard side for the tested wing configuration with a positive sweep angle (which would be inboard for a full-scale aircraft with a backward-swept wing). As a result, even if this point contributes less to the overall lift – being outside the propwash and closer to the wingtip – its proximity to the rotor enhances its effectiveness in influencing the inflow angle at the rotor disk. The tested configuration shown in Figure 4.2 has a positive sweep angle of $\Lambda = +27°$, with Figures 4.3 and 4.4 being respectively the unswept and opposite sweep configurations. These last two were not tested experimentally and both use the same spanwise distribution of circulation as the positively swept case, with the unswept case not having its circulation corrected for the reduction in sweep angle, as the comparison intends to highlight the differences due to the location of the lifting line, rather than the same wing at different sweep angles, as in that case the propwash would also need to be considered.

For this reason, the wing's effectiveness at inducing upwash on the rotor, the red line of Figures 4.2 to 4.4, is calculated as the increase in induced inflow angle at the disk centre for a given constant circulation distribution over the wingspan.

This distribution provides insight into which wing sections contribute most to the upwash at the rotor and how they interact with the propwash. The spanwise circulation distribution is influenced by several factors, primarily the wing's vertical offset and longitudinal distance from the rotor. These factors affect the lifting line's influence on the rotor through different mechanisms: for the wing, distance is relevant due to the r^2 dependency in the Biot-Savart law, while for the propwash, the effect is aerodynamic, driven by wake diffusion and variations in the rotor wake impinging on the wing depending on their relative vertical offset. Any alignment of the circulation peaks with those of the propwash, which intensifies inflow non-uniformity across the rotor disk, is thus mainly dependent on the relative position of the rotor with the wing. Consequently, even small geometric adjustments can mitigate inflow peaks or reshape them to optimise propeller performance.

For the tested configuration, the wing sweep is the main factor driving inflow non-uniformity, as the geometric shift due to sweep brings parts of the lifting line much closer to the rotor than the mean distance. Since the influence scales with the square of the distance, even small sections of the wing can have a significant effect on the inflow angle. Moving the wing downstream would broaden the peak of the red curve, as the effectiveness would drop more at the closest point than at neighbouring sections. However, if the peak of inflow effectiveness remains centred with the rotor axis, the overall inflow distribution could stay relatively symmetric. The second factor shaping the distribution is the presence of the propwash, which locally changes the wing section's incidence angle, causing sharp increases and decreases in lift over an area approximately matching the rotor diameter.

The following figures show the circulation over the wingspan for the positive sweep angle configuration, with the same circulation distribution applied to all three cases. The effectiveness at inducing upwash varies across the span, highlighting the influence of different wing sections on the rotor inflow. The rotor contour plot depicts the change in inflow angle relative to the predicted value at the rotor centre, which is the geometric angle α_G plus the correction α_C. The deviation in effective inflow angle from the centre is normalised by the maximum α_G tested in the dataset.

The tested positive sweep configuration represents the worst case for inflow non-uniformity, as the peak effectiveness aligns with the peak circulation. With the starboard side of the wing closer to the upgoing side of the rotor, it generates the most intense upwash, significantly increasing the inflow angle and reducing the blade incidence angle in the already least loaded part of the rotor. This effect is exacerbated by the fact that upgoing blades tend to experience a greater loss in loading than the downgoing blades for the same inflow angle variation.

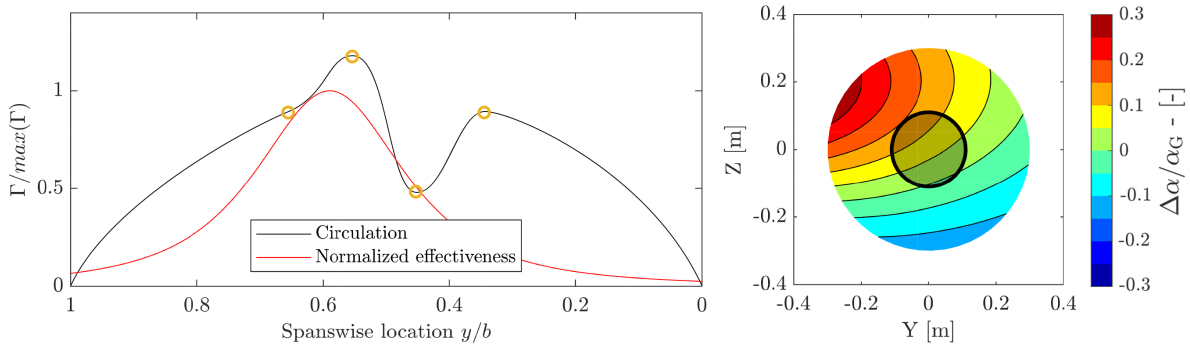

Figure 4.2: Intermediate α_G, intermediate thrust setting, TO_3 β_p, $\Lambda = +27°$.

For the unswept configuration, the wing effectiveness is more symmetric, reducing the strong lateral gradient observed in Figure 4.2, with only a slight asymmetry remaining due to the non-uniform circulation over the wing. While any potential performance benefit from a more uniform rotor inflow is overshadowed by the hugely degraded wing performance, this highlights that the wing circulation itself is only partially responsible for the lateral inflow non-uniformity at the rotor.

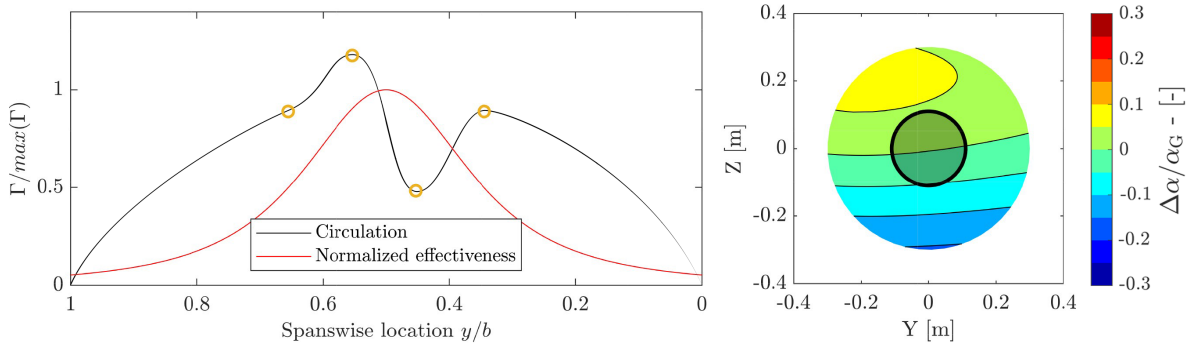

Figure 4.3: Intermediate α_G, intermediate thrust setting, TO_3 β_P, $\Lambda = 0°$

It is evident how having the upgoing blade nearest to the leading edge, as in Figure 4.2, strengthens the inflow gradient at the rotor compared to the opposite rotation shown in Figure 4.4.

The difference between the two cases is amplified by the fact that the upgoing blade near the leading edge is also the retreating blade, experiencing a stronger decrease in α than the increase observed by the advancing blade in the opposite configuration. This behaviour, combined with the self-induced velocities from preceding blades, can lead to an even more pronounced non-uniformity in the disk loading.

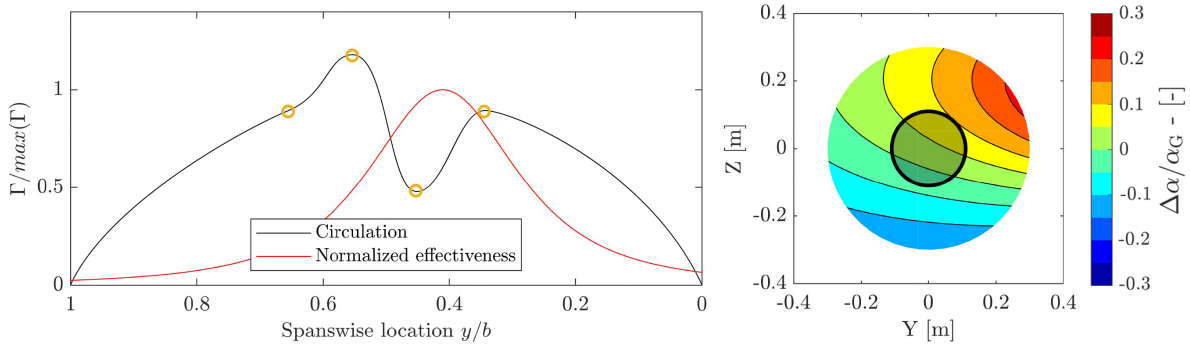

Figure 4.4: Intermediate α_G, intermediate thrust setting, TO_3 β_p, $\Lambda = -27°$.

One possible solution to the inflow non-uniformity, which could be problematic depending on its inter-

action with many other engine parameters, could be the use of inboard-down rotating engines. While this approach could help reduce the asymmetry of the inflow, it would come at a higher cost in terms of both maintenance and manufacturing due to the asymmetry in engines between the port and starboard wings. Given the uncertainties surrounding the effects of inflow non-uniformity, this solution may not be cost-effective. The impact of the non-uniformity on overall performance is still not fully understood, and further investigation is required to determine the actual benefits. If the effects are less significant than expected, the added complexity and expense of outboard engines may not be justified. In any case, the tested configuration represents the worst case for the scaled demonstrator in terms of the deviation in blade loading between the downgoing and upgoing blades.

4.1.5. Effective inflow angle

The influence of the advance ratio on wing lift, and consequently on the inflow correction, is evident as a trend where higher thrust levels correspond to higher lift at the wing and thus at higher corrections α_C. However, this effect is partially obscured by the presence of multiple wing configurations with different leading-edge devices, as the correction also depends on the wing geometry. Figure 4.5 shows the inflow correction applied to all wing-on data, with different values of geometric angle of attack α_G grouped together to show the dependency on the thrust setting of the rotor.

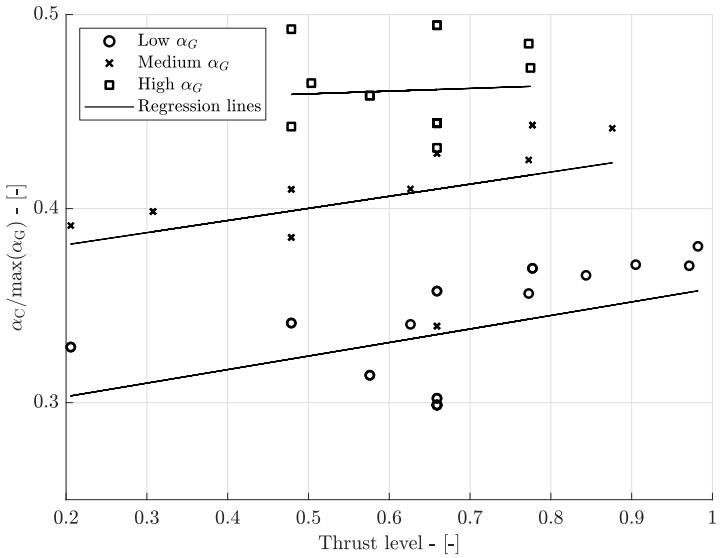

Figure 4.5: Normalised increase in inflow angle α_C at the rotor centre as a function of thrust setting with TO_3 β_p.

Higher thrust levels contribute to the inflow angle at the rotor by increasing the dynamic pressure in the slipstream, which in turn increases the circulation in the most effective part of the wing at generating upwash. However, this effect is less significant than the angle of attack, which has a greater influence on lift. In high-angle-of-attack configurations, the lift-induced increase in inflow (α_C) can reach up to 50% of the geometrical angle of attack α_G.

The thrust-induced effect is secondary to the angle-of-attack-induced inflow in terms of the average induced inflow. However, it plays a more significant role in shaping the nonlinear inflow component, particularly due to the wing sweep and the resulting deviation from the elliptical distribution of circulation. The difference in inflow correction between low and high thrust settings can range from 15% to 25% of the total correction, depending on the specific wing configuration, including the presence of leading-edge devices and flaps.

4.2. Bending quantification

To quantify the deformation, the mean y-displacement is evaluated over a defined region of the blade, spanning from 45% to 55% of the chord and from 65% to 75% of the blade span, which corresponds to

75% to 85% r/R. This approach mitigates potential inaccuracies associated with selecting a single mesh point while avoiding regions near the leading and trailing edges, which are more susceptible to outliers. The spanwise location is chosen to be in the middle of the linear part of the bending profile, as visible in Figure 4.7, far from any curvature while still a region of the blade where the chord is wide enough and allows to average over more meshpoints.

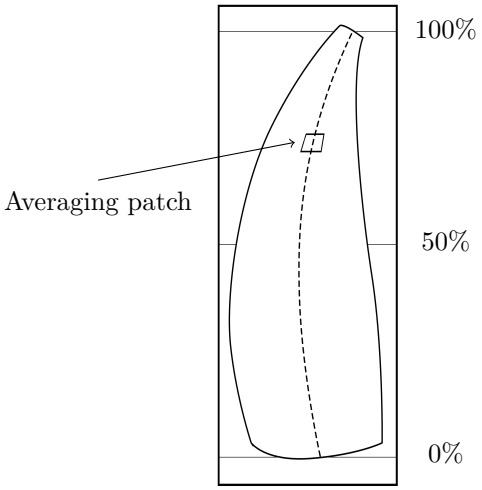

Figure 4.6: Averaging patch and 50% chordline from which the values used in the regressions are obtained. The sketch is simply indicative and does not represent accurately any blade geometry.

The bending over the span at the 50% chord line shows strong similarity between the most and least loaded cases, as shown in Figure 4.7. The bending profiles of the two cases nearly overlap, differing only by a linear scaling factor. This suggests that despite the variations in loading, the fundamental shape of the bending response remains remarkably consistent across the span.

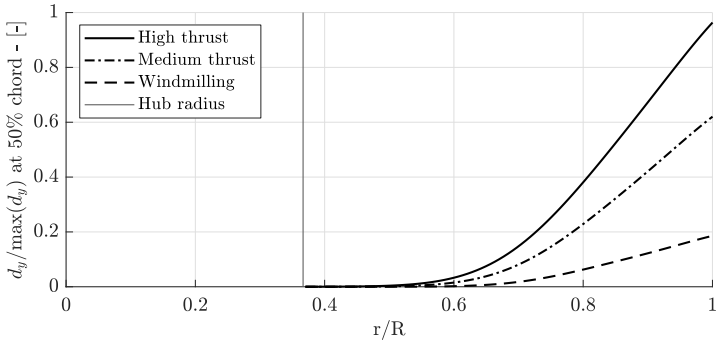

Figure 4.7: Non dimensional blade bending over the span on the 50% chordline.

What is also visible in the bending line are the three blade sections with different profiles. From 37% to 50% r/R the blade has zero deformation, and that is approximately the reference area. Between 50% and 75% r/R there is the curvature region, which is the only section of the rotorblade which has a positive second derivative of the displacement with respect to the radius, the remaining tip region is in fact linear other than some inaccuracy exactly at the tip due to the small measurement area.

5

Deformation Analysis

Two sets of data are used for the analysis: the first dataset consists of variable azimuth measurements and is aimed at finding changes in the periodic behaviour of the blade deformation under different loading conditions, such as a rotation of the azimuth at which the maximum bending occurs for the rotor. The second dataset is instead composed in total of 140 points, and is used to fit a regression model and analyse the resulting deviation between the wing-on and wing-off predicted deformations at blade azimuths $\varphi = 53°, 238°$, with assumptions based on the results obtained from the first.

5.1. Test data and measurement methodology

The advance ratio, J, is defined as

$$J = \frac{V}{nD} \tag{5.1}$$

and is primarily governed by changes in rpm, with velocity playing a lesser role since the Mach number remained constant at 0.2 throughout the testing campaign. Thus any velocity variations were due to fluctuations in air temperature and humidity.

All data points were recorded at fixed corrected rpm values (rpm_C), ensuring consistent blade tip Mach numbers for a given rpm_C. However, the actual uncorrected rpm varied slightly due to the same changes in temperature and humidity affecting the Mach number.

Three rotor pitch angles were used in the test, corresponding to differently loaded cases of take-off. These are called TO_1, TO_2 and TO_3, with the pitch $\beta_1 < \beta_2 < \beta_3$. While using the corrected rpm_C value simplifies thrust scaling and aeroacoustic analysis, it introduces an error in the centrifugal loads on the propeller. Given the active cooling of the wind tunnel and minimal temperature fluctuations during testing, the difference between rpm_C and rpm was assumed negligible and was not accounted for in the analysis discussed in this thesis. The first dataset consists of one polar without the stator blades and two with the stator set at high incidence angle. All three have a common rotor pitch equal to the TO_1 setting and are in wing-off condition. The other points analysed with a variable blade azimuth are taken from the second dataset in order to use data which had the same engine parameters used for the other analysis. The second dataset is divided into wing-on and wing-off cases and further classified by rotor pitch, each set respectively for TO_1, TO_2 or TO_3 take-off configurations, with all points sharing the same constant stator angle, which is lower than in the first dataset. Initially, the analysis focused on the downgoing blade, but preliminary results indicated that maximum loads and lift-induced upwash occurred for the TO_3 rotor pitch data due to the design of the test matrix. Consequently, two additional subsets of the upgoing blade measurements were selected for further evaluation, while data for TO_1 and TO_2 was excluded from the C34 camera system analysis due to time constraints.

The evaluated datapoints for the TO_3 pitch setting are shown in Figure 5.1, as function of the thrust setting and the effective inflow angle, normalized by the maximum geometric one.

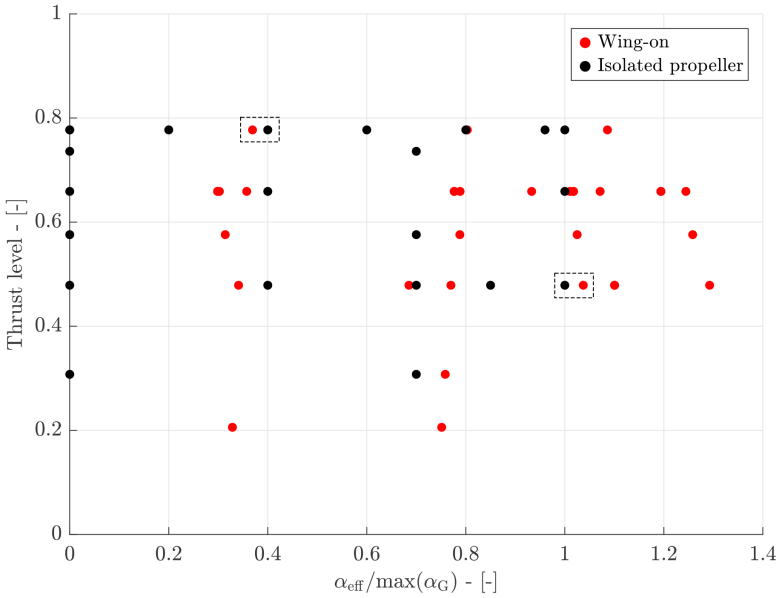

Figure 5.1: Distribution of datapoints for TO_3 blade pitch, normalized against the maximum geometric angle of incidence. The four points in the dashed rectangles are chosen for the analysis in section 5.4.

To comprehensively characterise rotor deformation, a series of measurements were conducted under varying aerodynamic conditions, each designed to address specific aspects of the fluid-structure interaction.

The first measurement is done at a variable rotor azimuth with a 1° resolution, spanning over two stator passages with the measured rotor blade seeing two different stator blades in the measured range. Its scope is to quantify the effect of the stator on the rotor at a low advance ratio, so at the highest thrust setting, as the stator deformation is maximised for that condition meaning that the stator loading and induced rotor loading must also be. As the rotor is not imaged at the same azimuth relative to the stator blades for C12 and C34, it is necessary to quantify the effect of any phase shift on the rotor deformation due to periodic stator induced loading.

The azimuthal measurement position for the wing-off, $\alpha_G = 0°$ case did not introduce significant bias. Since the stator has no effect on the measured data, the measurement location relative to the stator does not introduce any error, as it does not influence the inflow or aerodynamic characteristics in the analysed configuration enough to give a measurable effect in the rotor bending. First the wing-off, stator-off cases at zero and high α_G are analysed to locate the azimuth of maximum displacement and to verify the symmetry in deformation under uniform inflow aligned with the thrust axis. Second four polars, both wing-on and wing-off configurations at low and high corrected angles of attack, each sampled at eight distinct azimuths over two relative stator passages, are evaluated. The objective is to identify the azimuthal position corresponding to the maximum deformation in both configurations, in order to evaluate the relative position of the images taken by C12 and C34 with respect to the periodic loading, allowing for a direct assessment of the impact of lift-induced upwash.

The primary focus is the effect of non-uniform inflow on rotor deformation. It is hypothesised that variations in inflow distribution would alter the azimuthal position of maximum displacement. Given that the C12 and C34 camera positions in the wing-off case capture the mean deformation—C12 observing the downgoing trend near the mean, and C34 the upgoing trend—any shift in the azimuth of maximum displacement would result in measurements capturing different phases of the periodic loading, thereby affecting the interpretation of deformation patterns. This is shown in Figure 5.2, where the dashed lines indicate respectively the azimuth measured by C12 on the left and C34 on the right. The measured value is quite similar between the two due to the approximately opposite azimuth and the alignment with the mean bending.

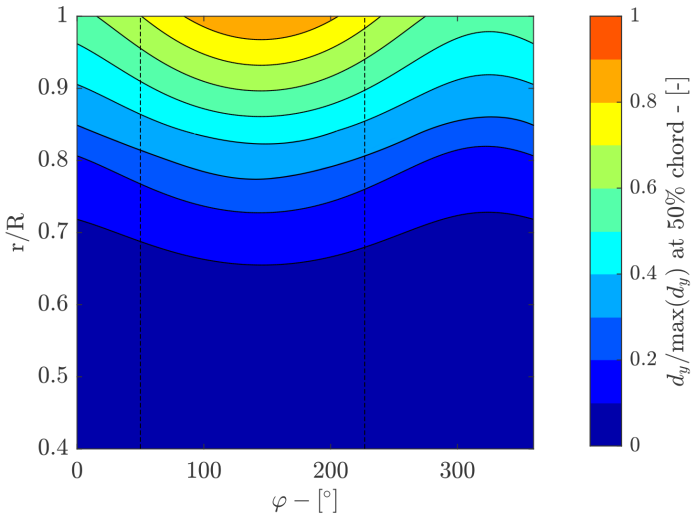

Figure 5.2: Normalised predicted rotor disk deformation for high α_G, high thrust,$T0_1$ β_p. The dashed lines indicate the measurement azimuth of C12 (left, $\varphi = 53°$) and C34 (right, $\varphi = 238°$).

At last the largest dataset is used to produce four fitted models, one for each combination of wing-on, wing-off and C12, C34, in order to predict the deviation in bending due to the wing presence. The analysis of these deviations is based on the results obtained from the previous study.

5.2. Stator Effects on the Rotor

The first measurement aimed at capturing azimuth-dependent deformation was conducted at the end of the testing campaign. Images were sequentially acquired with a 1° offset, covering a 100° range with 100 images. A significant challenge was the use of two cameras to observe the same blade from different perspectives across this extensive set of blade positions. As the azimuth deviated from the optimal viewing angle, the common field of view shared by both images decreased.

Reflections present in one image but absent in the other further constrained the usable dataset, limiting the range to approximately 60° or two blade passages. This still represented an improvement over the single passage measurement provided by the images originally taken for the stator measurement. To accommodate the extended azimuth range, the reference area at the blade base was reduced to maintain consistency across all images despite changing perspectives.

This approach involved a notable trade-off. Unlike the other variable azimuth method, where measurements were averaged over 50 samples, each azimuth position now depended on a single image, reducing overall accuracy. The smaller reference area also diminished the influence of the rigid-body transformation, affecting precision for the . Although this method is not optimal due to the reduced measurement quality, single measurements provide higher accuracy but cannot capture the rotor's deformation dependency on the relative stator position.

The data consists of a single polar and spans approximately two stator passages. Conducted at a zero angle of attack and in a wing-off condition, the resulting bending is expected to be independent of the blade azimuth. This assumes that the stator's influence on the rotor deformation is negligible, owing to the blade's response time to the periodic loading it experiences. The induced loading frequency ranges between $800Hz < BPF < 2000Hz$ for advance ratios $2 < J < 0.9$. While the unsteady normal force increases with thrust, the necessary reduction in advance ratio corresponds to a rise in loading frequency, resulting in no discernible impact on the displacement field unless a particular eigenfrequency is matched.

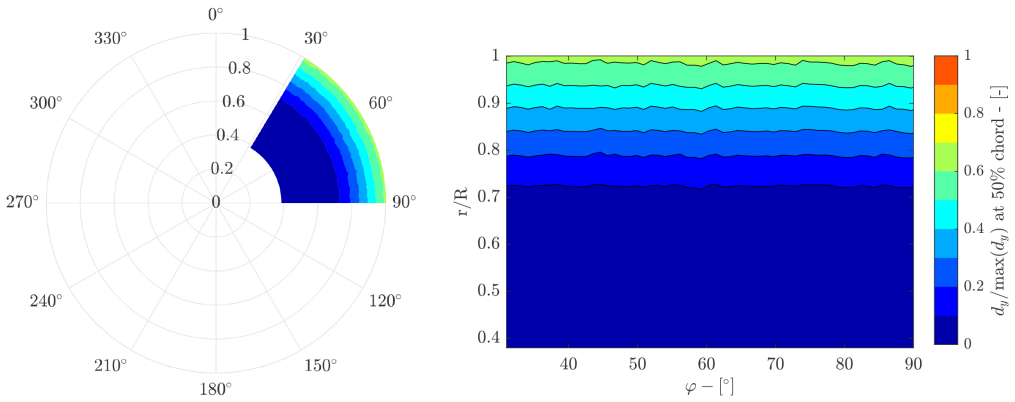

Figure 5.3: Normalised rotor bending at 50% chord over two stator blade relative passages, 1° azimuthal resolution, $\alpha_G = 0°$, high thrust, TO_1 β_p.

The periodic loading imposed by the stator on the rotor is primarily influenced by the number of blades, their geometry, and the distance between the rotor and stator planes. For the APIAN propeller with SRVs the unsteady normal force shown in Figure 5.4 ranges between $0.8\% < c_n' < 2.3\%$ of the time-averaged coefficient across various thrust settings (Sinnige et al., 2018), and considering the presence of 14 blades rather than 6, no significant effect of the stator on rotor deformation is expected.

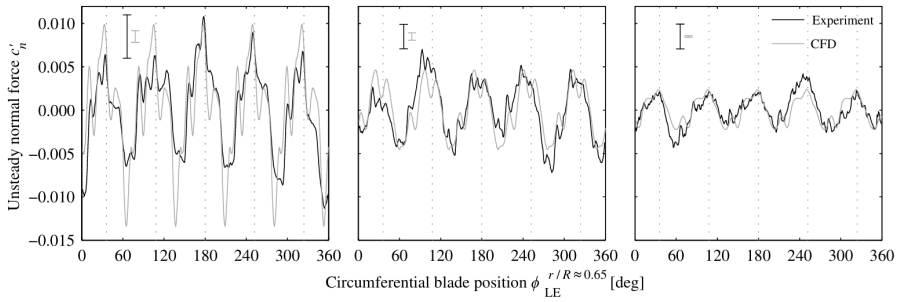

Figure 5.4: Unsteady rotor loads on the six-bladed APIAN model with SRVs at r/R ≈ 0.65 (High thrust / Intermediate thrust / Low thrust) (Sinnige et al., 2018)

The variable azimuth measurement serves thus primarily to verify the absence of phase dependency in the $\alpha = 0°$ case. This ensures that results of the two camera groups, measured at different phases relative to the stator position, are free from systematic errors related to the phase alignment.

A notable limitation is the significantly reduced number of image pairs available for any rotor azimuth — fifty times fewer than in the stator-off case, with the advantage of covering twice the area of the disk with a six times higher angular resolution. This reduction substantially diminishes the accuracy of the measurement, but removes the need to perform the interpolation, which would not be possible anyway over more than one 80% of a stator passage due to the available image data.

The results in Figure 5.3 show no dependency of the rotor deformation on the azimuth relative to the stator blades, excluding then any systematic bias between the measurements of the two stereo groups.

5.3. Isolated Rotor Deformation

To verify the symmetry in deformation at a $\alpha_G = 0°$ angle of attack and identify the azimuth angle corresponding to the maximum displacement at a high angle of attack multiple measurements at different azimuths were taken, allowing to interpolate in between the data. The following results are derived from the wing-off and stator-off configuration. Although no measurable effect from the stator was

observed, the baseline tests with eight azimuth positions were conducted in the stator-off configuration to eliminate any potential influence. The blade loading for the APIAN rotor with a uniform angular inflow is sinusoidal with a 360° period, peaking at approximately 120°, as shown in Figure 2.6, and so the peak in deformation is also expected slightly later than for $\varphi = 90°$. In Figure 2.6, the maximum is given at a different azimuth due to the different reference system, with $\beta > 0$ and $\varphi = 30°$ corresponding to $\alpha > 0$ and $\varphi = 120°$. The azimuth of maximum loading is independent on the advance ratio, but it does depend on the blade pitch β_p as found experimentally. The isolated rotor behaviour matches between Figures 5.9 and 5.10 at TO_3 β_p, where the maximum deformation is off by 6°, which is within the accuracy of the fit, but it does not coincide with the azimuth found for TO_1 β_p in Figure 5.6.

Each polar includes eight bending profiles, with four profiles per stereo group, one for each measured azimuth. A boundary condition ensured zero deformation at the blade root ($r/R \approx 0.4$). A piecewise nonlinear model, defined as two different polynomial fits for $0.4 < r/R < 0.7$ and $0.7 < r/R < 1$ is used due to the distinct profile geometry (Figure 4.7). The coefficients of the two polynomial fits are a function of φ and are periodic.

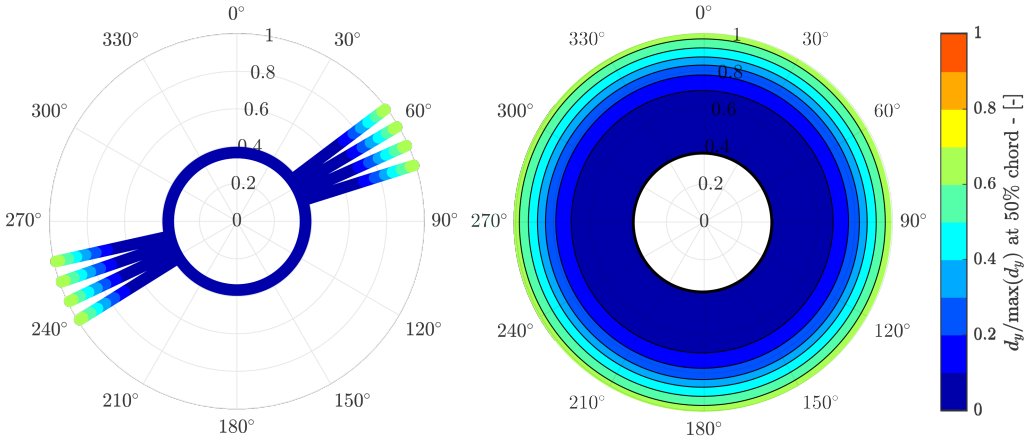

Figure 5.5: Normalised rotor disk deformation, measured (left) and predicted (right), for $\alpha_G = 0°$, high thrust and TO_1 rotor pitch.

The second polar at high α_G with the TO_1 rotor pitch, is not directly comparable to the TO_3 data due to the different pitch and consequently due to the different thrust coefficient. This is even more valid when comparing it to other results such as those from the APIAN tests, where only the general characteristics can be assumed to be common.

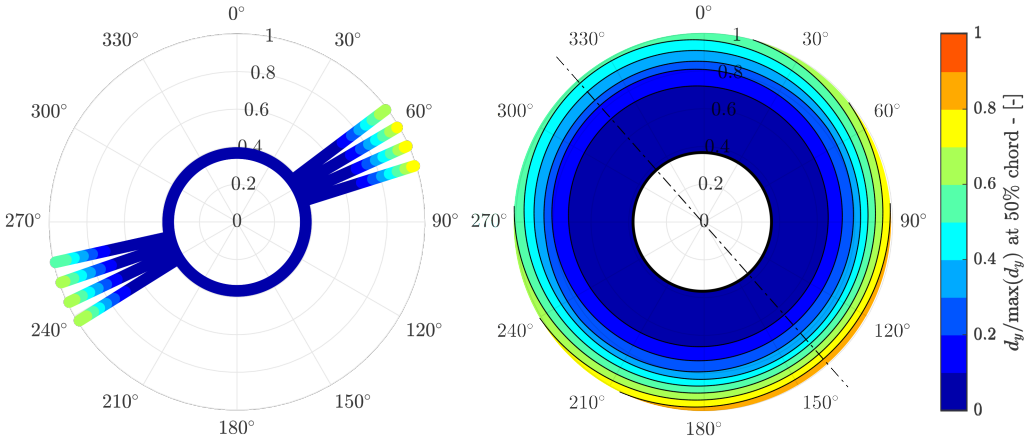

Figure 5.6: Normalised rotor disk deformation, measured (left) and predicted (right), for high α_G, high thrust and TO_1 pitch.

The dataset and boundary conditions are visualised in the polar scatter plot, with the fitted model predicting deformation across the entire rotor disk. The dashed line represents the symmetry axis of the bending distribution, determined from the phase coefficient of the sinusoidal fit.

As expected, the $\alpha_G = 0°$ polar of Figure 5.5 yields identical results regardless of blade azimuth. Interestingly, even at the high α_G setting in Figure 5.6, the two azimuths used for rotor imaging (the first of each four in clockwise order) exhibit nearly identical profiles. This goes back to the optimal azimuth being dependent on the blade geometry, and mostly on the position of the cameras and of the LEDs which were conveniently mounted on the side of the inlet nozzle on support beams mainly for ease of access and assembly. The notable result from these measurements is that the azimuth at which the maximum rotor bending is predicted is $\varphi = 142°$ for the TO_1 rotor pitch setting.

5.4. Wing Influence on Full Rotor Disk Deformation

Four additional polars are analysed similarly, with eight measurements per polar. They are selected to be as distant as possible in terms of thrust level and angle of attack, as shown in Figure 5.1, while maintaining a comparable angle of attack — either corrected for the wing-on configuration or the geometric angle for the wing-off cases. As the correction is always positive and consistent due to camber in the wing, the smallest common inflow angle with a difference smaller than 0.5° between wing-on and wing-off is at a intermediate α_{eff} setting, while the highest in common between the two is at a high α_{eff} one. The same limited range is present for the thrust setting due to the test matrix design and how the α_C corrections shift the points, with the two points having respectively high and intermediate thrust, but without any data from a low thrust setting polar.

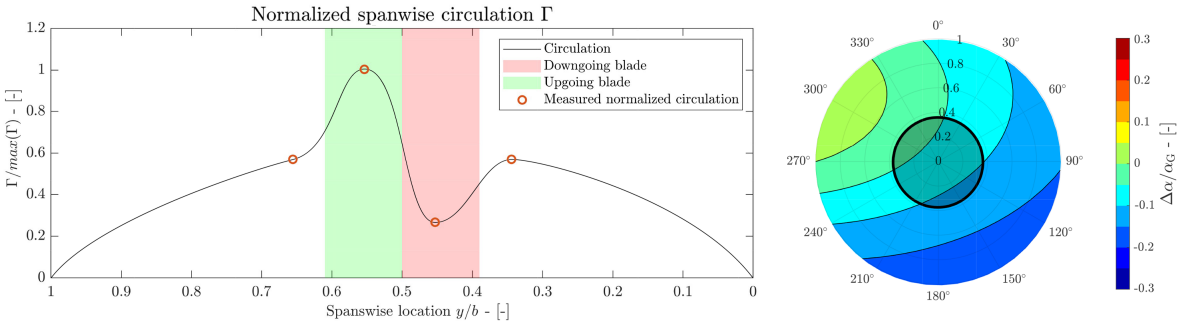

Figure 5.7: Normalized circulation and relative inflow distribution for the wing-on case at $\alpha_G = 0°$, intermediate α_{eff} case, normalised by the maximum geometric angle α_G.

The distributions of circulation shown in Figures 5.7 and 5.8, respectively at low and high α_{eff}, are normalized against the maximum predicted lift for engine off configuration, in the same way as for Figures 4.2, 4.3 and 4.4. The main focus remains on the inflow angle at the rotor rather than on the distribution that caused it.

The inflow angle is given in differential form when compared to the wing-off case chosen for comparison, which is the reason why the zero line does not pass through the centre of the rotor. The α_G of the isolated points does not perfectly match the α_{eff} of the wing-on ones at the rotor centre, so a small deviation of the zero line is present. Even if the effective inflow for the wing-on case is close to the geometric angle of attack of the isolated propeller, a small difference remains present. So while the comparison is not perfect, the effects of that deviation can be assumed negligible for the purpose of the analysis.

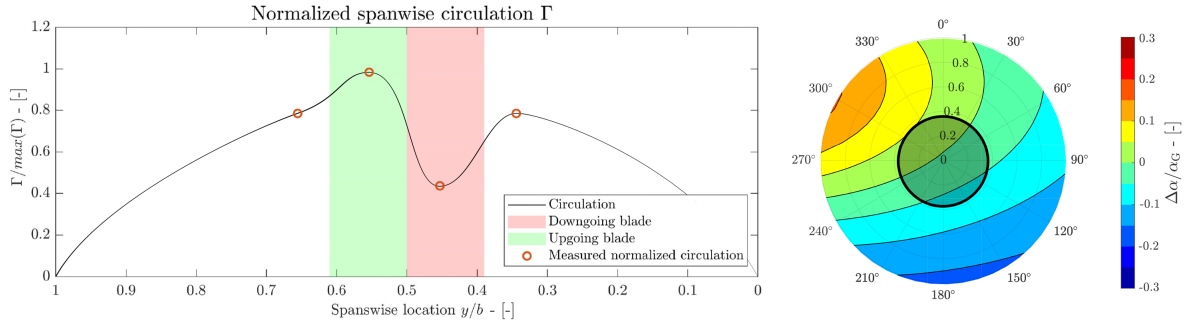

Figure 5.8: Normalized circulation and relative inflow distribution for the wing-on case at intermediate α_G, high α_{eff}, normalised by the maximum geometric angle α_G.

The lateral asymmetry in the wing induced inflow gradient influences the bending over the rotor by introducing smaller periodic effects resulting in a final distribution that is not a simple sinusoid with period equal to 360°, but due to the limited amount of measurement locations it is not possible to obtain any higher-order model for the deformation.

The vertical gradient in inflow angle induces an increase in loading for $0° < \varphi < 90°$ and $180° < \varphi < 270°$, while causing a reduction in loading for the remaining half, compared to a case with uniform vertical velocity across the disk. Due to the inherent symmetry, this variation does not result in a rotation of the deformation pattern but instead introduces a superimposed periodic effect with half the period observed in the wing-off configuration.

Due to the inflow distribution, the expected rotor behaviour in the wing-on configuration is as follows: the blade at $\varphi = 135°$ experiences a smaller load increase due to reduced inflow, while the opposite blade at $\varphi = 315°$ encounters stronger upwash, reducing its loading. Conversely, the blades at $\varphi = 45°$ and $\varphi = 225°$ experience higher loading, as the advancing blade is exposed to increased upwash in this configuration.

Thus, the phase shift of the fit is the sole parameter analysed. While it does not fully capture the deformation behaviour across the entire disk, it is expected to reflect the unaccounted portion of the inflow non-uniformity, which corresponds to the flow field after subtracting the uniform gradient and mean value.

Using the same model as in Figures 5.5 and 5.6 the eight measurements and the root boundary conditions are used to predict the bending.

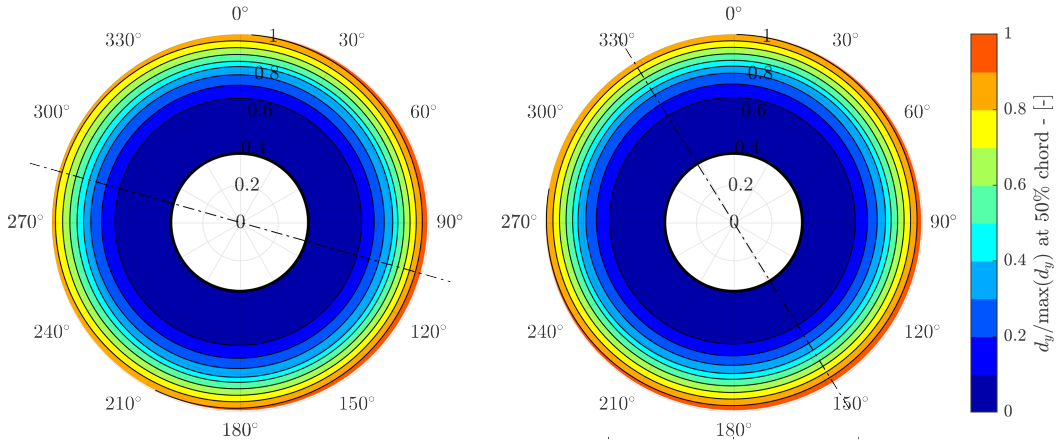

Figure 5.9: Normalised rotor disk deformation for wing-off at intermediate α_G(left), and wing-on at intermediate α_{corr}(right), high thrust setting, TO_3 rotor pitch.

Both comparisons reveal a clockwise rotation of approximately 45° in the azimuth of maximum bending due to the wing presence, which cannot be attributed to the vertical inflow gradient (Figures 5.9 and 5.10). The variation in inflow angles from $\varphi = 180°$ to $\varphi = 0°$ is approximately equal for both the high and low α_{eff} polars at 60% of the mean angle. However, this effect should not manifest as a rotation.

One possible cause lies in the upgoing blade at $\varphi = 315°$, near the point closest to the wing leading edge, which experiences the greatest upwash and thus undergoes the most significant loading loss compared to the changes occurring across the entire rotor. This loss in loading is considerably greater than the gain at $\varphi = 135°$, due to the higher velocity closer to the wing, as well as the general tendency for upgoing blades to lose more loading than the downgoing blades gain.

The downgoing blade at $\varphi = 53°$, measured by C12, lies along the $\Delta\alpha = 0$ contour line (Figure 5.7) which corresponds to the same upwash as the wing-off condition, even if here it is caused by the sweep angle and the asymmetric nature of the inflow. This aligns well with the observed deformations, where wing-on and wing-off conditions exhibit nearly identical values at $\varphi = 53°$ for equivalent α_{corr} and J.

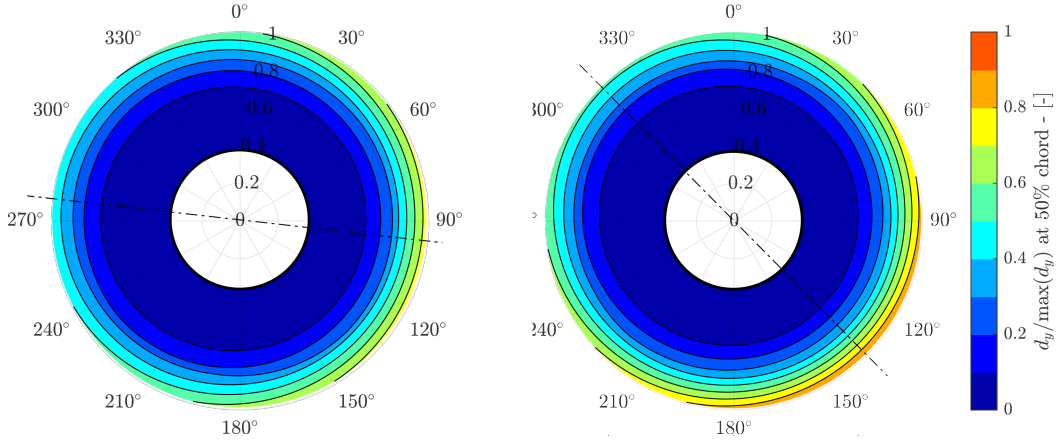

Figure 5.10: Normalised rotor disk deformation for wing-off at high α_G (left), and wing-on at high α_{eff} (right), intermediate thrust, TO_3 rotor pitch.

At a lower thrust setting the same considerations apply, with the azimuth of maximum bending being rotated clockwise by $\approx 45°$. The maximum inflow angle is located again at $\varphi \approx 315°$ and so is the minimum bending, while at $\varphi = 53°$ the inflow angle is the same as the wing-off case (Figure 5.8), with no significant deviation between the two measured deformations.

5.5. Wing Influence Analysis Over Model Operating Range

The test data showed that the rotor pitch $\beta_p = TO_3$ exhibited the widest range of model angles of attack, α_G, and the largest variations in deformation at 80% r/R, while also corresponding to the lowest thrust settings among the three tested pitches. This dataset was selected for analysis in both isolated and wing-on conditions, across both azimuthal locations, as fitting the data would be easier and more accurate compared to the other rotor pitches, which covered a smaller portion of the operating range.

The data is fit on four separate models for the upgoing/downgoing blades and wing on/clean cases, shown in Figure 5.11. The deformation is modelled as a function of the thrust level T_{lvl}, the non dimensional effective mean angle of attack $\alpha_{\text{eff}}/\max(\alpha_G)$, their interaction term $T_{\text{lvl}} \cdot \alpha_{\text{eff}}/\max(\alpha_G)$, and the quadratic term T_{lvl}^2. For the regression the standard deviation of the bending over the 100 image pairs is used as a weight. Its value is averaged over the same patch used for the deformation, as shown in Figure 4.6.

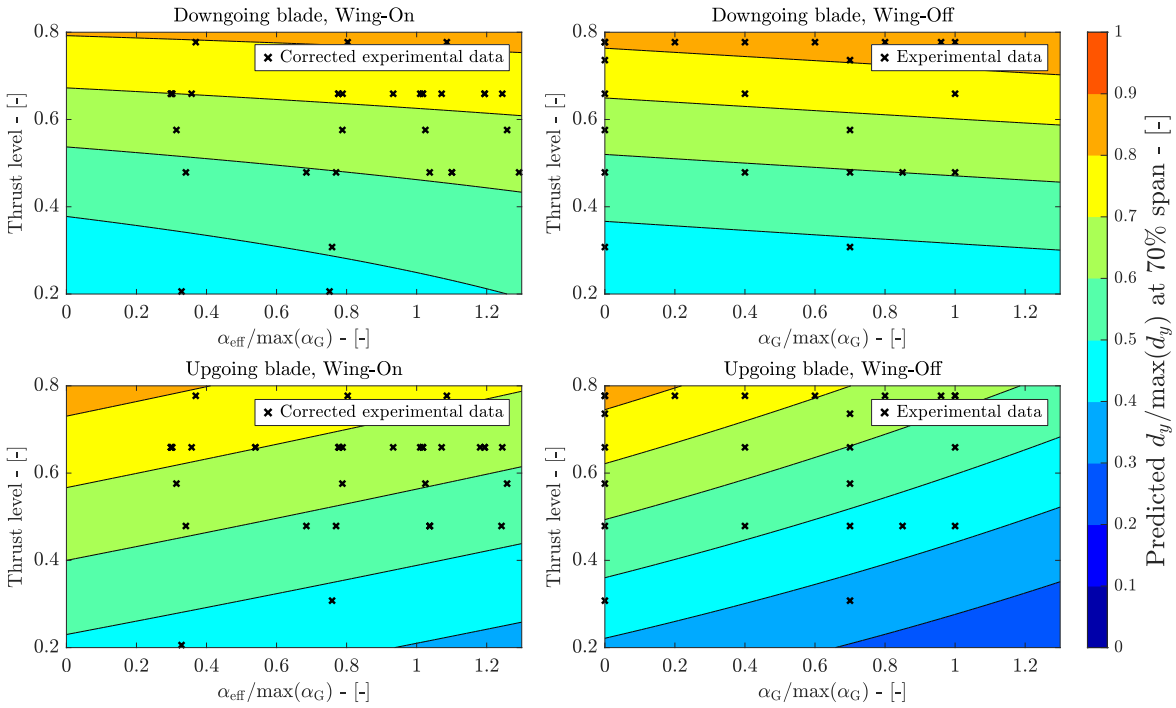

Figure 5.11: Normalised predicted bending models for both blade positions and wing configurations, TO_3 rotor pitch.

One thing to note is that the measurements out of C34 do have a slightly higher standard deviation, but other than obvious outliers which have been removed manually the results adhere to the quality standards and are not technically worse. Vibrations could for example increase the standard deviation of the bending, and with most of the C34 data having a $0.3mm < \sigma(d_y) < 0.5mm$, more than double that of C12 with $0.1mm < \sigma(d_y) < 0.2mm$, it could simply be the case.

In Table 5.1 the coefficients of the models are shown, with the thrust setting having the most effect on deformation as expected.

Table 5.1: Summary of Regression Results for the TO_3 rotor pitch setting.

Configuration	T_{lvl}	α_{eff}	$T_{lvl} : \alpha_{\text{eff}}$	T_{lvl}^2	R^2	$RMSE$
Downgoing, Wing on	0.156	0.048	-0.044	0.210	0.994	0.044
Downgoing, Clean	0.152	0.010	0.019	0.237	0.999	0.027
Upgoing, Wing on	0.316	-0.046	-0.015	0.018	0.956	0.069
Upgoing, Clean	0.364	-0.057	-0.072	0.062	0.955	0.042

For C12 (downgoing blade, $\varphi = 53°$) both wing-on and isolated results show a minimal dependency on the inflow angle with the contour lines that are almost horizontal; at the upgoing blade this is not true, with higher inflow angles strongly reducing the local loading and thus the bending. This behaviour is confirmed by Figures 5.9 and 5.10, where the location measured by C12 at $\varphi = 53°$ is deformed very similarly between the isolated and wing-on case. At the opposite azimuth, $\varphi = 238°$, measured by C34, the presence of the wing increases the local deformation. The four polars analysed in Figures 5.9 and 5.10 span a substantial part of the operating range (Figure 5.1), suggesting that this behaviour, with the downgoing blade being almost unaffected and the upgoing instead being subject to greater loading due to the wing's presence, can be traced back to the same rotation in the deformation pattern, without having to go through the much more intensive process used for the full disk interpolations, which required four times as much data.

The deviation between the corrected wing-on regression and the isolated data shows in Figure 5.12 the good quality of the correction, with an increase in thrust dependency towards higher inflow angles. This means that the azimuth measured by C12 is approximately a fixed point in the deformation pattern, as it is almost independent on the wing presence and the thrust setting.

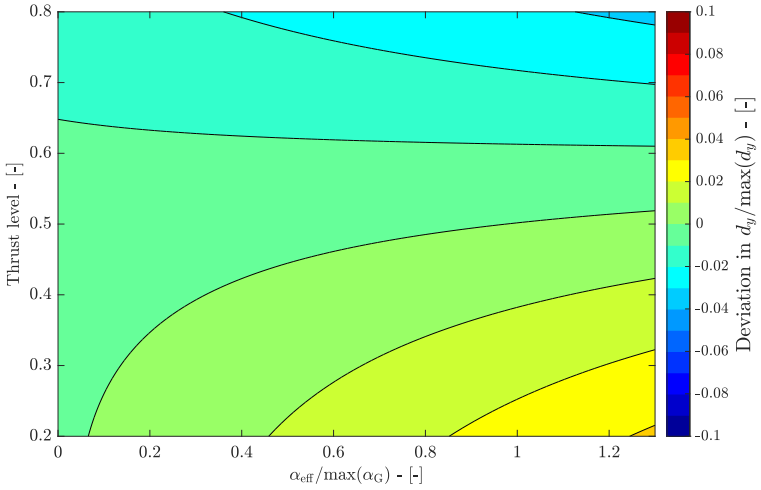

Figure 5.12: Normalised Deviation of the corrected wing-on data from the wing-off data for downgoing blade at $\varphi = 53°$.

This deviation for the upgoing blade dataset is also shown in Figure 5.13, where the difference of the two bending predictions is given. The results are much different from the ones from the opposite azimuth, with the sensitivity being higher for the inflow angle than for the thrust setting.

The main effect for $\varphi = 238°$ that makes the dependency on the mean effective inflow angle so high, is not the angle itself but rather the consequences it has on the lift distribution of the wing and thus on the non uniformity of the inflow.

It is important to note that the deviation at $\varphi = 238°$ is positive and significant not only due to a mean increase in deformation magnitude under wing-on conditions caused by the altered inflow, but also due to a phase shift in the bending distribution. As the deviation measured by C12 remains approximately null across the entire range of T_{lvl} and α_{C}, and given that C12 and C34 are positioned at opposite azimuths, the deviation observed by C34 is effectively double the mean increase for a given T_{lvl}-α_{C} setting.

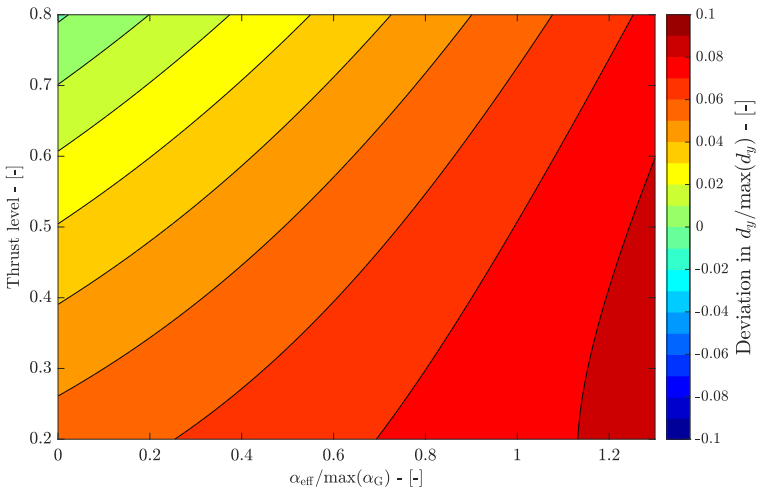

Figure 5.13: Normalised deviation of the corrected wing-on data from the wing-off data for upgoing blade at $\varphi = 238°$, TO_3 pitch setting.

The normalized mean deformation increase across the rotor disk caused by the presence of the wing is approximately 0.05 $d_y/\max(d_y)$ at high effective angle of attack and the lowest thrust setting. When compared to the isolated data, this corresponds to an effective deformation increase of about 10% due to the wing presence. However, this increase diminishes as the angle of attack decreases, due to the reduction in upwash magnitude. Additionally, as the advance ratio increases, the higher induced velocities become more dominant in influencing the rotor loading, overshadowing the relatively small nonlinear inflow component. This results in a decrease in the effect of the wing on the deformation at higher advance ratios and lower angles of attack.

The 10% increase in mean deformation compared to the isolated data arises from how the inflow angle correction is applied. Increasing the correction value would shift the wing-on raw data to the right in Figure 5.11, altering the computed deviations. However, the relative change between the two measured azimuths would remain unaffected. A higher correction value would reduce the positive deviation at C34, while lowering the deformation at C12. In this case, a different correction could produce results where the deviation at C34 becomes null, while C12 shows a negative deviation. This confirms that the uniform inflow correction influences only the mean deformation level, without affecting the phase or the symmetry axis of its distribution.

5.6. Stator deformation under different thrust settings

The following section presents the deformation measurements of the stator blades under three distinct rotor operating conditions: windmilling, low thrust, and high thrust. The steps taken to capture the images necessary for the evaluation of the surface are explained later in Appendix A, as well as all the image processing and flash setup.

These measurements, illustrated in Figure 5.14, give some insight into the aerodynamic behaviour of the stator and the corresponding structural response. The measured displacement d_y across the blade span shows a smooth and continuous field, of similar accuracy and quality to the rotor measurements, despite the suboptimal conditions. The consistency between the deformation patterns and the expected aerodynamic loads further validates the quality of the results, as they align well with the measured torque and thrust coefficients of the stator.

Only these three polars were evaluated as part of the thesis for the stator setup, as the much greater stiffness of the stator blades compared to the rotor gave a lower range of motion and thus more relative uncertainty.

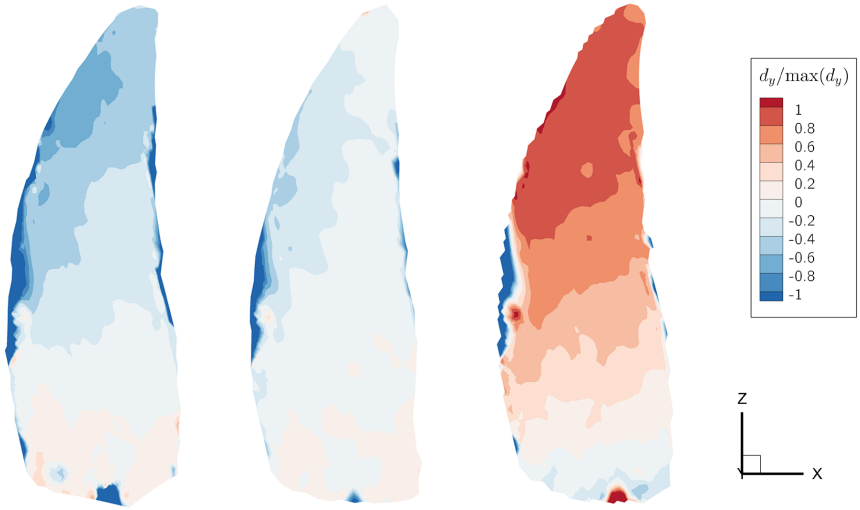

Figure 5.14: Stator deformations for the windmilling (left), low thrust (middle) and high thrust (right) rotor settings, normalised by the maximum stator y-displacement. - (Digitally distorted surface)

When the rotor is windmilling the stator stalls due to the reduced rotor swirl which results in an incidence angle that is negative, and the load is aligned downstream. The resulting bending is slightly negative, so towards the pressure side of the stator. In the low thrust setting instead the flow is attached and it greatly reduces the drag component with respect to the windmilling case, this results in a minimum deformation at the stator blade. At high thrust instead the strong swirl component in the flow results in a higher incidence angle at the stator, which in turn generates more lift and bends the blade up to the maximum measured displacement at the tip towards the suction side.

6

Conclusions

The initial questions guiding this research were:

1. *How does the lift-induced upwash from a downstream wing affect the rotor and stator deformation of an upstream engine?*
2. *To what extent does the inflow angle correction, derived from lift-induced upwash models, enable wing-on data to correlate with wing-off deformation measurements?*
3. *How does the inflow distribution caused by sweep affect the deformation dynamics of the rotor and the reliability of the correction methods?*

The lift-induced upwash generated by a downstream wing modifies the inflow conditions experienced by the upstream engine, leading to changes in rotor deformation. This upwash locally increases the tangential velocity at the blades and alters their incidence angle across the rotor disc, introducing asymmetric loading. As a result, the rotor blades exhibit variations in bending depending on their azimuth, particularly at higher lift conditions where the upwash effect is more pronounced. The extent of these deformations depends on the aerodynamic interaction between the wing and the rotor, as well as the structural properties of the blades.

The equivalence between geometric and lift-induced upwash for a wing without sweep and no vertical offset from the thrust axis was demonstrated in previous experiments. The decomposition of the upwash into its mean, vertical gradient, and non-linear components revealed that when the mean component dominates and the inflow remains largely uniform, the resulting deformation closely matches that of the isolated configuration at the same effective angle of attack. In a case where only $\varphi = 53°$ is measured, no deviation would have been present between the wing-on and wing-off configurations. Conversely, with measurements only at $\varphi = 238°$, the deviation would have been double the mean increase due to the specific effect the tested wing had on the rotor.

The stator deformation dependency on lift-induced upwash was not analysed due to time constraints, as it required processing twice the amount of data as the rotor. While the stator measurements successfully resolved the occlusion issue, they were only used to correlate with the rotor thrust setting.

The applied α_C inflow corrections to the deformation measurements proved effective, even in the presence of wing sweep. The uncorrected non-linear component of the inflow manifested as a significant deviation between the wing-on and wing-off cases at a specific measured azimuth. The use of interpolations, which required data from multiple azimuths, performed across equivalent wing-on and wing-off data points allowed the identification of its effect on rotor disk deformation. However, in a different test setup—such as one using a single stereo group or two groups positioned differently—these deviations might be indistinguishable from measurement errors, as to measure the rotation of the symmetry axis and the increase in mean bending it is necessary to have measurements at different azimuths.

Furthermore, the limitations regarding the wing positioning in the test campaign prevented a more comprehensive assessment of the impact of lift-induced upwash. The original planning included varia-

tions in the longitudinal and vertical wing positions, which were not tested, restricting the scope of the analysis. While not perfect, the angle of attack corrections proved to be a step in the right direction, even if the inflow non-uniformity was not accounted for in the correction.

Despite these limitations, several key observations were made. The propwash had a measurable influence on the wing lift and induced angle of attack, confirming its significance in the aerodynamic behaviour of the system. The azimuth of maximum bending was measured both in the clean and in the wing-on configurations. The effects of the three components of the inflow—divided into mean, linear vertical, and non-linear components—were observed as an increase in the amplitude of the primary sinusoidal deformation, a non-measurable second-order sinusoid, and a phase shift in the first-order sinusoid, respectively.

Regarding the third research question, it was found that the non-linear component of the inflow, primarily caused by wing sweep and further amplified by propwash, influenced rotor deformation dynamics in ways that could not be fully captured with measurements taken at only two opposite azimuths. The interplay between local inflow distortions and the blade's dynamic response introduced complex deformation patterns beyond what a simple sinusoidal model could describe. A shift in the deformation pattern of up to 45° was observed, along with a mean bending increase—calculated at 70% of the blade span across all azimuths—of approximately 10%.

This deviation depended strongly on the interaction between wing-induced inflow and rotor self-induced velocities. As the angle of attack increased, so did the wing-generated lift, leading to stronger upwash effects that further altered the inflow distribution. Similarly, at higher advance ratios, the decrease in rotor thrust reduced self-induced velocities relative to the wing-induced upwash, amplifying the non-linear deformation effects.

Additionally, the limited azimuthal resolution and strong reflections from the blade geometry constrained the ability to resolve finer spatial variations in the deformation field. Since measurements were largely aligned with the mean bending direction, local inflow distortions could not be fully captured. The presence of a vertical inflow gradient, while theoretically relevant, remained unquantified due to the 180° phase shift of the two camera groups, which made it impossible to measure its effects.

Overall, these findings highlight that the non-uniform inflow distribution introduced by wing sweep leads to both phase shifts and amplitude variations in rotor deformation, which cannot be fully accounted for using a simple sinusoidal model. Future studies incorporating additional azimuthal measurement points and refined inflow models could improve the accuracy of correction methodologies.

Regarding the stator instead, this test demonstrated the feasibility of employing digital image correlation to measure the partially occluded stator surface, under the assumption that the rotor wake does not influence its deformation. The image alignment process, required to reconstruct a complete image from multiple partial views, proved effective due to the minimal random component of the in-plane shift of 6mm and the considerable camera-to-surface distance of 9m. In cases involving shorter focal lengths or increased positional uncertainty, this process could become considerably more challenging.

For configurations with more flexible blade geometries or a counter-rotating open rotor (CROR) engine, where the occluded surface is also in motion, alternative solutions would be required. Whenever possible, the most reliable approach remains direct surface measurement. In this case, achieving that would have required painting the pressure side of the stator and installing four additional cameras downstream of the model.

6.1. Implications for future work

The most effective way to advance this research would be to investigate the effects of different wing sweep angles, both positive and negative, on rotor deformation. Additionally, capturing surface measurements at more than two azimuth positions, avoiding placements that are exactly opposite to each other, would provide a more comprehensive understanding of the deformation behaviour.

Future research could also benefit from the integration of strain gauges with IPCT, though the use of strain gauges presents challenges, as they must be embedded within the blade layup, limiting their accessibility and placement. However, employing a smaller number of strategically placed strain gauges could still allow for effective correlation with IPCT data, enabling the generation of more complete deformation fields over the entire disk, even in regions where IPCT is constrained by shadows or optical limitations. This approach would enhance the accuracy of deformation maps and improve the overall analysis, at the cost of a complex calibration necessary to correlate the discrete strain values with the deformation field.

Additionally, investigating the relationship between in-plane loads, as measured by the RSB, and the bending and twist over the disk could offer more precise insights into rotor dynamics. Together, these methods could address the limitations observed in the current study.

To build on this research, further testing with varying wing positions and sweep angles would be the most promising direction. Incorporating refined measurement techniques, such as higher-density IPCT coverage, strategically placed strain gauges, and enhanced inflow characterization, would improve the accuracy of deformation analysis and contribute to a deeper understanding of rotor-wing interactions in aerodynamic systems.

References

Guynn, M. D., Berton, J. J., Haller, W. J., Hendricks, E. S., & Tong, M. T. (2012). *Performance and environmental assessment of an advanced aircraft with open rotor propulsion* (tech. rep.).

Hoff, G. (1990). *Experimental performance and acoustic investigation of modern, counterrotating blade concepts* (tech. rep.).

Negulescu, C. A. (2013). Airbus ai-px7 cror design features and aerodynamics. *SAE International Journal of Aerospace*, *6*(2013-01-2245), 626–642.

Stürmer, A., Gutierrez, C. O. M., Roosenboom, E. W., Schröder, A., Geisler, R., Pallek, D., Agocs, J., & Neitzke, K.-P. (2012). Experimental and numerical investigation of a contra rotating open-rotor flowfield. *Journal of Aircraft*, *49*(6), 1868–1877.

Sutcliffe, P. L. (1987). *The boeing 7j7-the evolution of technology and design* (tech. rep.). SAE Technical Paper.

Li, Q., Wang, Y., & Eitelberg, G. (2016). An investigation of tip vortices unsteady interaction for fokker 29 propeller with swirl recovery vane. *Chinese Journal of Aeronautics*, *29*(1), 117–128.

Avallone, F., van den Ende, L., Li, Q., Ragni, D., Casalino, D., Eitelberg, G., & Veldhuis, L. (2019). Aerodynamic and aeroacoustic effects of swirl recovery vanes length. *Journal of Aircraft*, *56*(6), 2223–2235.

Dring, R., Joslyn, H. D., Hardin, L., & Wagner, J. (1982). Turbine rotor-stator interaction.

Veldhuis, L. L., Kotsonis, M., & van Berkel, E. (2013). Non-uniform inflow effects on propeller performance. *31st AIAA Applied Aerodynamics Conference*, 2801.

Alba, C., Elham, A., German, B. J., & Veldhuis, L. L. (2018). A surrogate-based multi-disciplinary design optimization framework modeling wing–propeller interaction. *Aerospace Science and Technology*, *78*, 721–733. https://doi.org/https://doi.org/10.1016/j.ast.2018.05.002

Veldhuis, L. L. (2004). Review of propeller-wing aerodynamic interference. *24th International Congress of the Aeronautical Sciences*, *6*(1), 2004–6.

Sinnige, T., Ragni, D., Eitelberg, G., & Veldhuis, L. L. (2016). Pusher-propeller installation effects in angular inflow. *22nd AIAA/CEAS Aeroacoustics Conference*, 2875.

Ortun, B., Boisard, R., & Gonzalez-Martino, I. (2012). In-plane airloads of a propeller with inflow angle: Prediction vs. experiment. *30th AIAA Applied Aerodynamics Conference*, 2778.

Kirmse, T., Boden, F., Meyer, R., & Philipp, F. (2021, June). Wing deformation measurements for manoeuvres of high load at the airbus a320 dlr-atra by means of image pattern correlation technique [https://www.see.asso.fr/ETTC2021]. In ETTC (Ed.), *European test and telemetry conference proceedings online* (pp. 1–6). https://elib.dlr.de/145368/

Boden, F., Barth, H. P., Hein, S., Heitmann, D., Kirmse, T., Klein, C., Krüger, W.-R., Lemarechal, J., Norambuena, M., Schäfer, D., Schnell, R., Sinha, K., Theiß, A., & Weiss, A. (2023). Recent developments of common numerical methods and common experimental means within the framework of the large passenger aircraft programme (M. Fischer, Ed.) [E-ISSN: 1869-5590]. *CEAS Aeronautical Journal*, *14*(1), 281–293. https://elib.dlr.de/194746/

Kirmse, T., Maring, S., Schröder, A., & Ebel, P.-B. (2016). Image based fan blade deformation measurements on an airbus a320 v2500 engine in ground operation [AIAA 2016-0386]. *AIAA SciTech 2016*, 1–8. https://elib.dlr.de/99939/

Lanari, C., Stasicki, B., Boden, F., & Torres, A. (2013). Image based propeller deformation measurements on the piaggio p 180. *Advanced In-Flight Measurement Techniques*, 133–153.

Geeraert, A., & Stephan, C. (2015). CROR blade deformation, part 1: Experimental results by strain pattern analysis. *IFASD 2015*. https://hal.science/hal-01521880

Mauffrey, Y., Geeraert, A., & Verley, S. (2015). Cror blade deformation, part 2: Aeroelastic computations and comparison with experiments. *IFASD 2015*.

German-Dutch Wind Tunnels (DNW). (2025). Large low-speed facility (llf) [Accessed: 2025-02-04]. https://www.dnw.aero/wind-tunnels/llf/

Allied Vision. (2024). Bonito pro x-2620 camera details [[Online; accessed 01-Oct-2024]]. https://www.alliedvision.com/en/camera-selector/detail/bonito-pro/x-2620/

Cheng, H. (1978). Lifting-line theory of oblique wings. *AIAA Journal*, *16*(11), 1211–1213.

Sinnige, T., Stokkermans, T. C., Ragni, D., Eitelberg, G., & Veldhuis, L. L. (2018). Aerodynamic and aeroacoustic performance of a propeller propulsion system with swirl-recovery vanes. *Journal of Propulsion and Power*, *34*(6), 1376–1390.

A

Stator measurement setup

A.1. Stator Acquisition

While the deformation measurements on the stator were not the main target of this thesis due to their reduced loading and stiffer blades, work was done to solve the problem of the occlusion by the rotor blades. The optical occlusion necessitated multiple approaches, each with distinct assumptions and complexities.

Single Partial Exposure

This approach offers the simplest solution in terms of camera and acquisition system requirements, capturing a single image pair at a given rotor azimuth. No assumptions are needed, as every visible part of the pattern is imaged simultaneously at the exact rotor blade position. However, not all checkerboard markers are visible at once, depending on the model's angle of attack. Testing various combinations of rotor azimuth, model angle of attack, and rotor pitch to determine the optimal azimuth for image acquisition is impractical due to time constraints. Additionally, the rotor and camera geometry often result in only a small portion of the blade surface being visible in both cameras.

Multi-Flash Long Exposure

Using the STM, the camera exposure time can be set as a function of the rotor azimuth, ensuring that each exposure corresponds to the same number of blade passages (Figure A.1). Most of the light reaching the sensor comes from the flashes, which have fixed exposure settings, maintaining consistent image brightness across different rotor speeds despite the varying exposure times. The primary challenge is the flash refresh rate, which depends on rotor speed, sting movement, and potential blade deformation. This method assumes that deformation remains constant during one blade passage and that the sting remains stationary. If these assumptions hold, the images can be processed accurately.

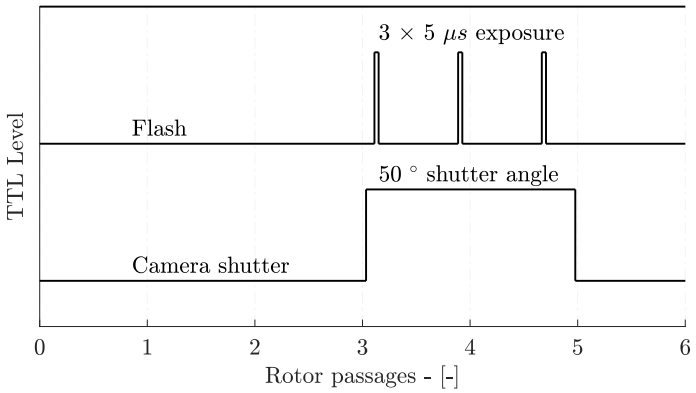

Figure A.1: Example of multi-flash long exposure for two blade passages and three flashes.

The main issue is with different parts of the stator being imaged a different number of times. This is shown in Figure A.2, where the surface is divided in different regions with the numbers representing how many times out of the three flashes each region is visible. Regions which are exposed only once present a darker but perfect pattern, while for regions illuminated two or three times the pattern does not match anymore due the sting movement. This of course introduces errors in the correlation.

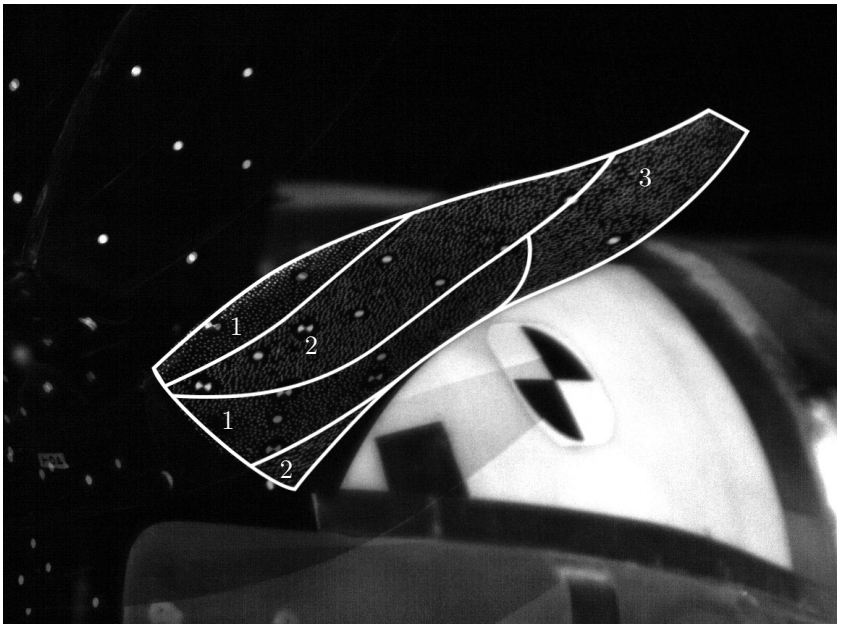

Figure A.2: Sting movement over one blade passage with four flashes every 6.5° of rotor azimuth, with the number of effective exposures per region overlaid.

Multiple Single Exposures with Digital Merging
This method mitigates flash refresh rate issues by acquiring images over different revolutions at the same rotor azimuths. It assumes constant deformation over one blade passage, while allowing sting movement. Image alignment is achieved using markers on the sting, with the assumption that the ratio of the image-plane shift to the camera distance is negligible. This enables compensation for sting movement through simple image translation, determined by cross-correlation of wing markers with sub-pixel accuracy between the first image pair and subsequent images, ensuring precise alignment without perspective distortion.

A.2. Stator image processing

Various assumptions had to be made in order to obtain a final image that could be analysed by the software.

The movement of the sting was the first issue in terms of image alignment. As the BPF was much higher than the flash refresh rate, it was not possible to take subsequent images in the same blade pass. This meant that although the relative position of the rotor to the stator was the same, the sting was in a different position, resulting in blurriness of the final stator image and in sharp edges between the regions. These edges arise from the black blades and shadows partially obscuring the dot pattern on the stator surface, leading to discontinuities between adjacent regions, as shown in Figure A.2, which were exposed a different number of times.

The second assumption is that the stator deformation is negligibly dependent on the rotor blade azimuth, both due to their stiffness and reduced radius which avoids strong deformations due to interaction effects with the tip vortices shed from the rotor. This would allow multiple images captured at different rotor phases to be optically averaged into a single, clean stator image over one blade passage. The resulting averaged image is assumed to represent the mean displacement during that passage.

The stator images are then processed as such to obtain a single complete image where the markers

and pattern are completely visible. The first step is to take images at different rotor azimuths (Figure A.3), in the case of the reference measurement this corresponds to 15 different positions, while during wind-on runs it is only 4, each at a quarter of a blade passing.

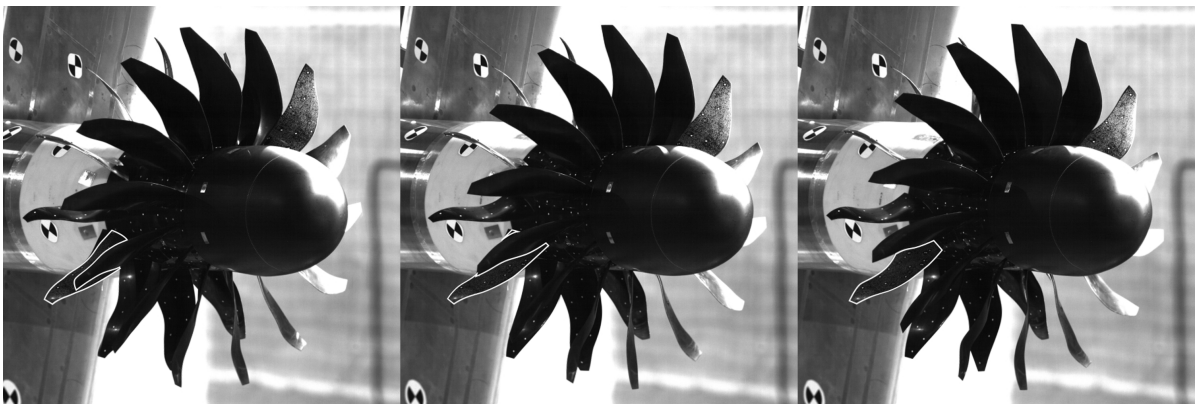

Figure A.3: Different rotor azimuths for the stator reference photos (Digitally distorted) with the visible stator region highlighted.

While the sting provides sufficient stiffness to hold the model steady, it lacks the precision required for measurements with an accuracy of less than 0.1 mm. To align the images, markers on the model in the background are used, referencing the first pair of images through a two-dimensional translation, as the deviation is consistently less than 20 pixels, even under full rotor power and Mach 0.2 conditions. In practice, this translation introduces no error, as the pattern aligns perfectly over the entire stator blade.

The next step involves masking the visible pattern portion of each image and calculating the average brightness pixel by pixel, with the sum of the masks serving as the denominator for the averaging. Blurring the edges of the masks reduces the hard borders caused by the varying shadows on the stator. At the root, where the apparent solidity is higher (i.e., a point is covered by a larger percentage of azimuths relative to the stator tip), fewer images have a clear visible area, resulting in lower SNR and more pronounced hard edges compared to the stator tip.

The resulting final image pair, after the alignment and masking, presents a clear stator blade, outlined in Figure A.4. In the same figure the areas affected by shadows and reflections, which caused problems for the rotor measurements, are visible at the top and right side of the image.

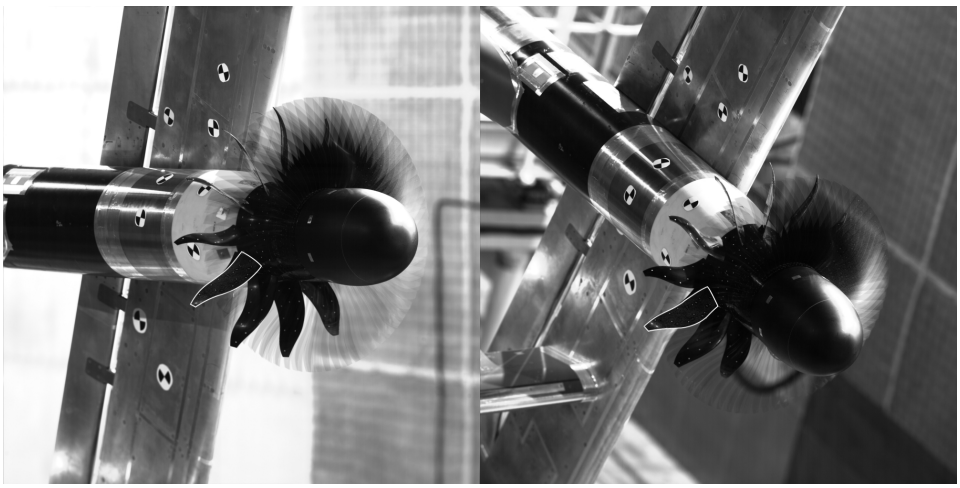

Figure A.4: Merged stator reference images, with the complete surface visible. - (Digitally distorted images)

An issue arose during the reference measurement due to the use of ambient light from the test section

lamps rather than high-power LEDs, leading to glare on the blades, visible in Figure A.5, which is a close-up of Figure A.4.

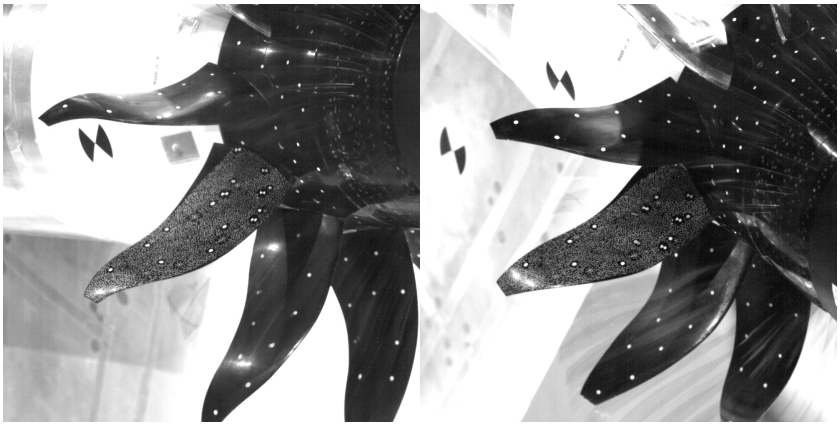

Figure A.5: Glare issue on the reference images - (Digitally distorted).

To address this, the Fourier transform of the image was calculated, and the wavelength associated with the glare was removed in spectral space before reconstructing the image, shown in Figure A.6. Although some portion of the glare remains visible near the tip, they are much smaller in size and the rest of the blade maintains a coherent pattern. While these remaining glared regions introduce errors in the computed reference surface, the triangulation error is significantly higher than the error introduced by the additional points. As a result, these parts of the surface can be excluded, leaving holes that can be reconstructed by interpolating the surrounding points.

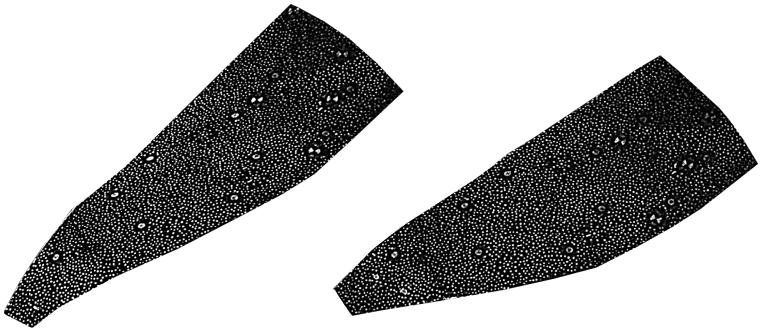

Figure A.6: Final reference image pair with the glare partially removed. - (Digitally distorted images)

The hot-shape measurements followed the same procedure of partial images being merged together but without any glare issue, as those were caused by the overhead lamps which were turned off during wind-on testing and not by the LEDs. Only a limited number of polars were evaluated, as no analysis could be conducted regarding the rotor blade passage or the C_T dependency. This limitation arose because the image merging process effectively captures data over a single blade passage, averaging results every $\approx 25°$. Nonetheless, the precise overlap of the partial images confirmed the absence of rotor-phase dependency in the stator deformation. If such a dependency had been present, it would not have been possible to exactly produce an image of the whole surface without any edge effects, which would manifest somehow similarly to the images shown in Figure A.2. In that case, an alternative method would have been required, though this was ultimately unnecessary.